Characterization and Application of Nanomaterials

VOLUME 3 , ISSUE 1 , 2020

1

ISSN: 2578-1995

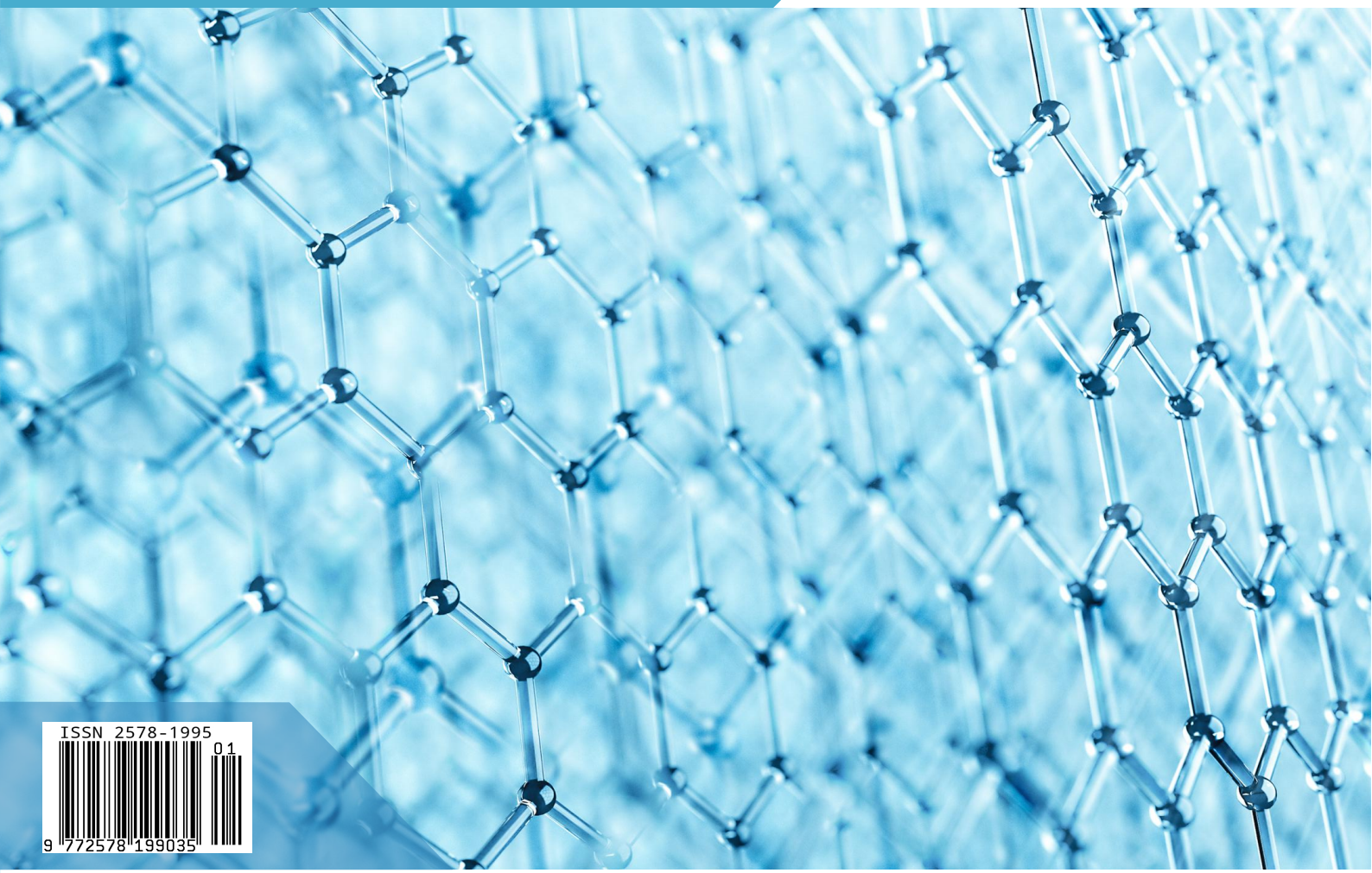

ISSN 2578-1995 01

9 772578 199035

EnPress Publisher

Editorial Board

Editor-in-Chief

Editorial Board Member

Volume 3 Issue 1 • 2020

Characterization and Application of Nanomaterials

EnPress Publisher

EnPress

2020 | Volume 3 | Issue 1

Characterization and Application of Nanomaterials

https://systems.enpress-publisher.com/index.php/CAN/

Contents

Characterization and Application of Nanomaterials (2020) Volume 3 Issue 1
doi:10.24294/can.v3i1.580

ORIGINAL RESEARCH ARTICLE

Effects of different preparing conditions and annealing on the photocatalytic activity of hydrothermal grown $BiVO_4$

Yuxiang Wen, Wei Ji, Jiang Yu, Qichang An, Tianfen Qin, Zhiya Zhang, Jiachi Zhang*, Shanglong Peng*

**Key Laboratory for Magnetism and Magnetic Materials of the Ministry of Education, School of Physical Science and Technology, Lanzhou University, Lanzhou 730000, Gansu province, China.*
**E-mail: pengshl@lzu.edu.cn. E-mail: zhangjch@lzu.edu.cn*

ABSTRACT

$BiVO_4$ was hydrothermally synthesized under different preparing conditions and characterized by XRD, SEM, Raman spectrum and BET specific surface area. The influence of different pH value and annealing temperature and hydrothermal time on the morphologies and structures of the $BiVO_4$ samples was investigated systematically. It can be found that annealing would eliminate the effects caused by the pH of precursor, heating temperature and heating time, but preparing conditions still influenced the size and specific surface area of samples. Furthermore, the photocatalytic activities of the fabricated $BiVO_4$ were also evaluated by the degradation of methyl blue in aqueous solution under UV and visible light irradiation.

Keywords: Bismuth Vanadate; Photocatalytic Activity; Morphology; Hydrothermal; Preparing Conditions

ARTICLE INFO

Article history:
Received 15 February 2020
Received in revised form 12 March 2020
Accepted 15 March 2020
Available online 27 March 2020

1. Introduction

With the huge consumption of traditional fossil fuels in the past several centuries, such as coal, crude oil and natural gas, human beings are now confronting a great energy crisis and environmental pollution issues. Accordingly, the development of semiconductor photocatalysts for organic pollutant degradation and water splitting has been regarded as an efficient, green and promising solution to energy replacement and environmental decontamination[1-5]. Among various semiconductor materials, TiO_2 has been regarded as one of the most promising photocatalysts owing to its large exciton binding energy, high chemical stability, non-toxicity and abundant availability[6,7]. However, its large band gap (~3.0 eV for rutile and 3.2 eV for anatase) means that TiO_2 is only active in the ultraviolet (UV) region, which accounts for less than 5% of the total energy of the solar spectrum[8,9]. In the past few decades, many researchers have focused their efforts on redeveloping visible-light-driven TiO_2-based photo-catalysts with high efficiency[10,11]. For example, Asahi *et al.*[12] and Khan *et al.*[13] reported that doping TiO_2 with nitrogen or carbon can narrow its band gap, and Putnam *et al.*[14] and Brezova *et al.*[15] reported that doping TiO_2 with metal ions extends light absorption into visible region. Nevertheless, as for the doped TiO_2 photocatalysts, the dopants may likely act as recombination centers for the photogenerated electrons and holes, resulting in lower quantum efficiency compared to undoped semicon ductor photocatalysts[16,17].

Bismuth vanadate ($BiVO_4$) has long been recognized as an important semiconductor photocatalyst, owning excellent photocatalytic performance under visible light illumination due to its narrow band gap (2.4 eV)[18-22]. There are three reported crystalline phases for synthetic $BiVO_4$, zircon structure with tetragonal system (z-t) and scheelite structure with monoclinic (s-m) and tetragonal (s-t) systems[23]. Therefore, many researchers focus their efforts on the photo-physical and photo-catalytic properties of $BiVO_4$ strongly influenced by its crystal form and preparation methods such as solid-state reaction[24,25], aqueous process[12,26-28], hydrothermal approach[29-32], chemical bath deposition[33,34], metal-organic decomposition[35], and sono-chemical method[35]. The architectural control of nano- and micro-crystals is an attractive and challenging goal of modern materials chemistry[36]. To this end, several exceptional structures, such as 1D $BiVO_4$ nanofibers, rod-like $BiVO_4$ and 2D $BiVO_4$ nanosheets, have been successfully fabricated by hydrothermal methods[37-39]. With these advanced processes, different surfactants or additives and complex treatments were necessary in order to obtain the desired morphologies and crystal structures[4,23,40,41]. Considering the properties and applications are closely related to the microstructure and corresponding synthetic techniques and processes, it is of great importance to study the controllable synthesis of $BiVO_4$ with the desired crystalline phase and morphology.

In this work, $BiVO_4$ has been synthetized by a hydrothermal approach. The photocatalytic activities of $BiVO_4$ prepared via different conditions were compared via the decomposition of methylene blue (MB) under UV and visible light irradiation. Also, the relationship between photocatalytic performance and fabrication parameters of $BiVO_4$ has been systematically investigated.

2. Experimental procedure

All the reagents used in the experiment are analytical grade without further purification.

2.1 Fabrication of $BiVO_4$

In a typical synthesis, 5.0 mmol Ammonium metava-nadate (NH_4VO_3) and 5.0 mmol Bismuth nitrate pentahy-drate ($Bi(NO_3)_3 \cdot 5H_2O$) were dissolved in 60.0 ml 1.0 M HNO_3 solution, stirring to obtain orange precipitate. The diluted ammonia water was then added for adjusting the pH value to 6. After stirring for 0.5 h, the solution was moved to 100 ml of Teflon-lined stainless steel autoclave and heated to 80°C, 100°C, 120°C, 140°C, 160°C, 180°C, and 200°C for 8 h under autogenous pressure, respectively. When cooled down to room temperature naturally, the yellow precipitate was obtained by centrifugation, wished with distilled water and absolute alcohol, and dried at 80°C in an electric oven for 8 h. The dried samples were heated from room temperature to 600°C at a constant rate within 2 h in the sintering furnace and annealed at 600°C for 2 h. After the temperature dropped to 300°C within 1 h, the samples were cooled down to room temperature naturally. The optimal preparation conditions were investigated by the influence of adjusting the hydrothermal temperature, the pH value of precursor (2, 4, 6, 8, 10, 12) and the hydro-thermal time (4 h, 6 h, 8 h, 12 h) on the photocatalytic activities.

2.2 Measurement of photocatalytic activities

Photocatalytic activities of the $BiVO_4$ powders were evaluated by the degradation of methyl blue (MB) under visible light irradiation ($\lambda > 420$ nm) using a 500 W Xe lamp with a 420 nm cut-off filter. In a typical run, 50 mg of samples was added to 50 ml of MB solution (1×10^{-5} mol/L). Prior to irradiation, the suspensions were stirred in the dark for 1 h to reach an adsorption/desorption equilibrium between the MB and photocatalyst. Under irradiation, the suspensions were stirred continually and open to air. At regular intervals, 4 ml of the suspensions were collected, and then centrifuged to remove the photocatalyst particles. These solutions were used to evaluate photocatalytic activities of the $BiVO_4$ powders by monitoring the absorbance at 554 nm with a UV-vis spectrophotometer (Shimadzu UV-3600).

2.3 Material characterization

The microstructure and morphology were investigated by using field emission scanning electron microscope (FE-SEM, Hitachi S-4800) and transmission electron microscopy (TEM, FEI Tecnai G2 F30 microscope operated at 300 KV). XRD measurements were performed on a Rigaku D/MAX-2400 X-ray diffractometer using Cu Kα radiation (λ = 0.154056 nm). The chemical component was analyzed on a micro-Raman spectroscope (JY-HR800, 532-nm wavelength YAG laser).

3. Results and discussion

3.1 Powders formation

The $BiVO_4$ samples were produced by the hydrothermal method and followed by annealing at 600°C. **Figure 1** shows the XRD patterns of $BiVO_4$ powders synthesized under different conditions. The difference in the XRD patterns between tetragonal and monoclinic $BiVO_4$ can be mainly judged by the existence of peaks (200) and (121) and the existence of a peak at 15°C and the split of peaks at 18.5°C and 35°C. The percentage of monoclinic phase can be given by the following equation:

$$\eta_{mono} = \frac{I_{mono(121)}}{I_{mono(121)} + I_{tetra(200)}}$$

Where η_{mono} denotes the percentage of the monoclinic phase, $I_{mono(121)}$ is the relative intensity of the (121) peak, and $I_{tetra(200)}$ is the relative intensity of the (200) peak.

As shown in **Figure1(a)**, $BiVO_4$ is monoclinic (PDF 75-1866) for the samples (c, d and e)[42]. As the pH decreases to 6 and 4, the tetragonal $BiVO_4$ appears (PDF 14–0133)[43]. These results indicate that the dissolution and the recrystallization happening in the low pH solution contribute to the phase transformation of the monoclinic type into the tetragonal type. The monoclinic $BiVO_4$ is thermodynamically more stable than that of tetragonal $BiVO_4$ at room temperature, and a sudden decrease in pH can affect the structure and morphology of powders resulting the formation of the tetragonal $BiVO_4$[44].

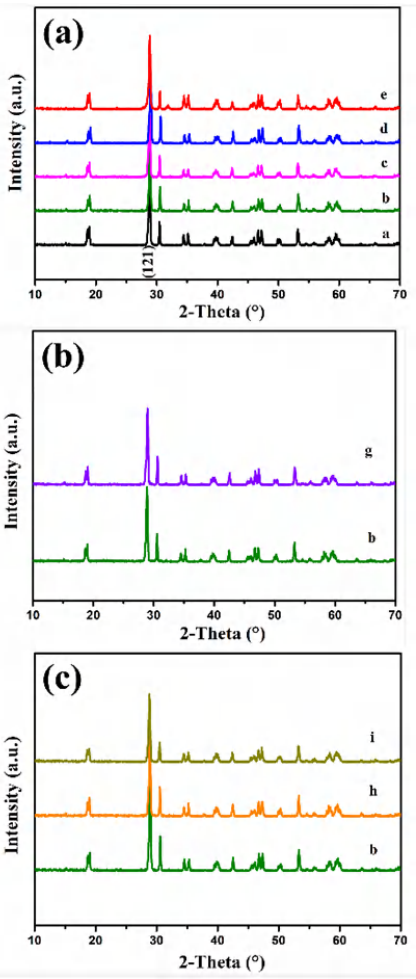

Figure 1. The XRD pattern of powders obtained from different conditions: **(a)** different pH values. **(b)** different heating temperature. **(c)** different heating time**.**

Similarly, as shown in **Figure 1(b)**, the samples (g and b) synthesized at 200°C and 180°C are monoclinic $BiVO_4$. As the temperature decreases to 160°C, the tetragonal $BiVO_4$ appears. Therefore, the $BiVO_4$ phase transition can be changed from monoclinic to tetragonal by adjusting preparation conditions. And the stable $BiVO_4$ is mainly related to the following chemical reactions[3]:

$Bi(NO_3)_3 + H_2O \Leftrightarrow 2HNO_3 + BiONO_3$

$BiONO_3 + VO_3^- \Leftrightarrow BiVO_4 + NO_3^-$

At the beginning, the reactants are soluble in concentrated nitric acid without precipitate. $Bi(NO_3)_3$ reacted gradually with water to form slightly soluble $BiONO_3$. And then, the newly formed $BiONO_3$ re-

acted with VO_3^-, forming yellow $BiVO_4$ powders. Furtherly, the samples without the high temperature annealing are a mixture of tetragonal and monoclinic $BiVO_4$. In **Figure 1(c)**, the samples (b, h and i) with different structure transit into monoclinic structure after high temperature annealing, indicating that $BiVO_4$ change from the tetragonal phase to the monoclinic phase by using high temperature annealing. **Table 1** shows the preparation conditions and percentage of monoclinic $BiVO_4$ powders (η_{mono}) of different samples, and the value of η_{mono} for each sample is 100%, which is accordance with the result in **Figure 1(c)**. The detailed parameters of these samples from different conditions are shown in **Table 1**.

Table 1. The preparation conditions and percentage of monoclinic $BiVO_4$ powders (η_{mono}) of different samples

Preparation conditions	a	b	c	d	e	f	g	h	i
pH values of precursor	4	6	8	10	12	6	6	6	6
Heating temperature (℃)	180	180	180	180	180	160	200	180	180
Heating time (h)	8	8	8	8	8	8	8	4	10
η_{mono} (%)	100	100	100	100	100	100	100	100	100

3.2 Morphologies and structure of the $BiVO_4$ samples

The chemical composition and molecular structure of the $BiVO_4$ samples were analyzed by Raman spectra as shown in **Figure 2** and **Table 2**. An intense peak near 828 cm^{-1} is assigned to the symmetric V-O stretching mode, and a weak shoulder near 707 cm^{-1} is assigned to the anti-symmetric V-O stretching mode. The short peaks located at 367 cm^{-1} and 324 cm^{-1} are assigned to the symmetric and the anti-symmetric banding modes of vanadate anion, respectively. The peaks near 210 cm^{-1} are assigned to the external modes (rotation/translation). With the increase of the precursor pH, these Raman peaks shift towards the lower wavenumber, which reveals that the short-range symmetry of the tetrahedral VO_4 becomes more regular[37]. Raman spectra are sensitive to the short-range order, the degree of crystallinity and so on. Therefore, Raman spectra embody the variation of preparation conditions. However, the Raman spectra of $BiVO_4$ samples prepared under different pH values change a little (**Figure 2**), which indicates the effects on the morphologies and structures of the samples can be eliminated by annealing at high temperature. These results are in accordance with the conclusion as shown in the XRD patterns. The strongest peak is located at the larger wavenumber and the value of the full width at half maximum is lower, indicating that the symmetry of tetrahedral VO_4 and the degree of crystallinity would be better after annealing treatment.

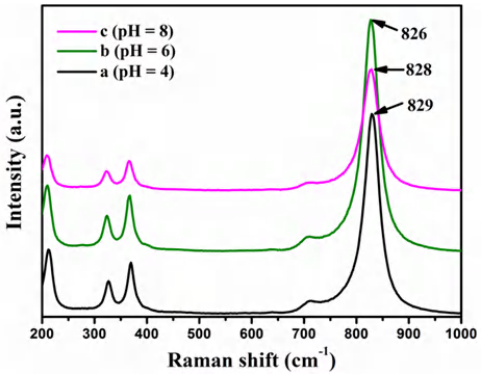

Figure 2. Raman spectra of the $BiVO_4$ samples prepared under different conditions.

Table 2. Assignment of Raman wavenumbers and specific surface areas observed from the samples obtained by hydrothermal method

Assignment	**Sample a (cm^{-1})**	**Sample b (cm^{-1})**	**Sample c (cm^{-1})**
ν_s (V—O) (FWHM)	829 (36)	827 (35)	829 (38)
ν_{as} (V—O)	711	709	712
δ_s (VO_4^{3-})	369	367	366
δ_{as} (VO_4^{3-})	326	324	322
External mode	212	210	210
A_{BET} ($m^2\ g^{-1}$)	2.57	2.65	2.59

Figure 3 shows the micrographs of the $BiVO_4$ samples prepared under different conditions. The samples present the similar morphologies of the peanuts-like particles after high temperature annealing corresponding to the analysis above. Nevertheless, it can be observed the difference between particles size and intensive degree. The results indicate the effects of reaction conditions on the structure and morphologies of the $BiVO_4$ samples can be eliminated by annealing, but these conditions still influence the particles size. The different specific surface areas of the

different samples are summarized in **Table 2**. The result also can reflect in SEM micrographs.

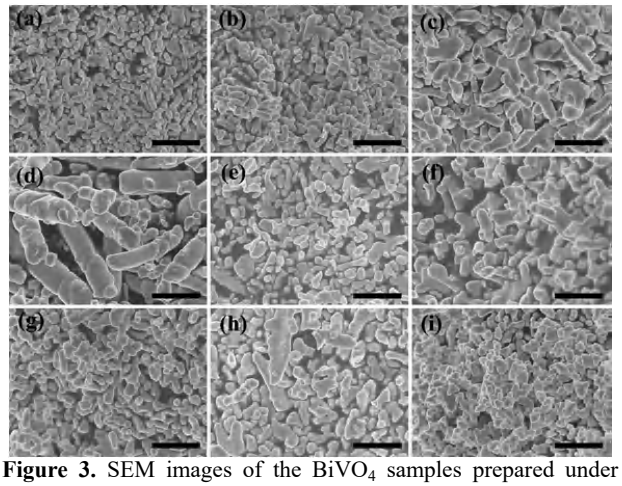

Figure 3. SEM images of the $BiVO_4$ samples prepared under different conditions, **(a)-(i)** corresponds to samples a-i in **Table 1**, respectively. The scale bar is the same for all 2 μm**.**

3.3 Photocatalytic activities

The photocatalytic activities of $BiVO_4$ samples were measured by the degradation of MB with a major absorption band at about 664 nm in a liquid medium under light irradiation.

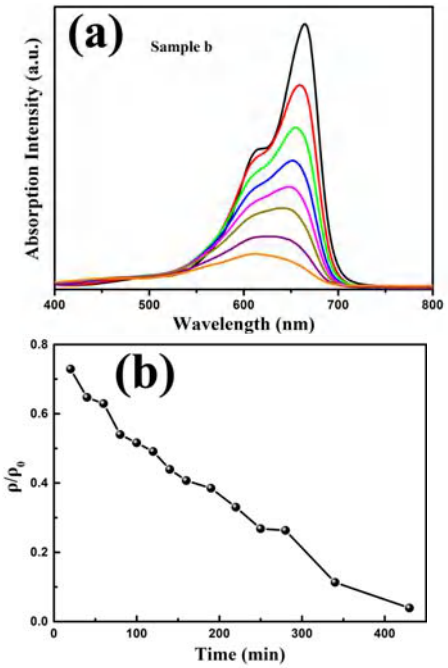

Figure 4. (a) UV-vis absorption spectrum of a stirred MB aqueous solution with the addition of sample b. **(b)** The photocatalytic degradation of MB in the presence of sample b with only visible light irradiation**.**

The temporal evolution of the spectral changes of MB mediated by the sample b, as shown in **Figure 4(a)**, exhibits that the absorption peak at 664 nm decreases gradually with irradiation time. Also the absorbance values of MB in the whole spectrum range from 400 to 800 nm are gradually reduced with increasing irradiation time, revealing the effectiveness and completeness of the photo-degradation of pollutants. **Figure 4(b)** presents the effect of degradation curve for the sample b under visible light irradiation (λ>420 nm), using a 500 W Xe lamp with a 420 nm cut-off filter. It can be observed that the monoclinic $BiVO_4$ has the ability of direct photolysis of MB as the increase of irradiation time.

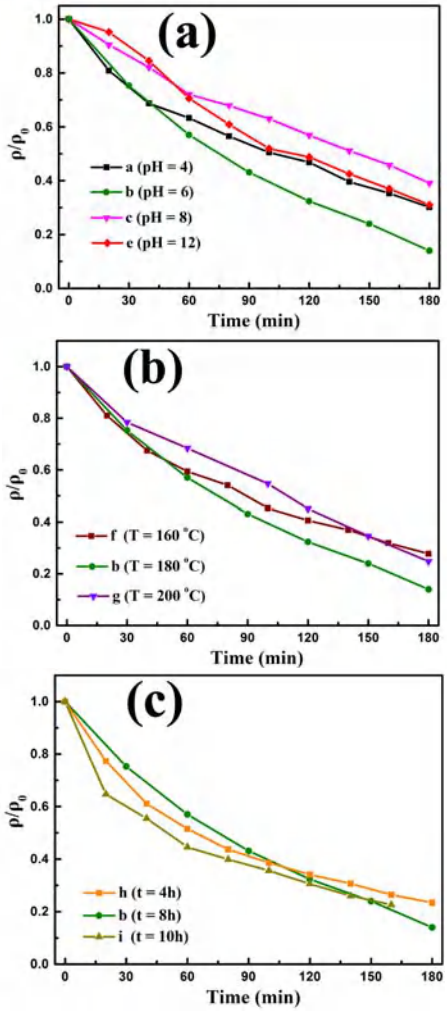

Figure 5. The photocatalytic degradation of MB with only visible light irradiation in the presence of different samples prepared under different conditions: **(a)** different pH values; **(b)** different heating temperature; **(c)** different heating time**.**

Figure 5 shows the photocatalytic activities of different samples fabricated under different conditions. These curves reveal that the concentration of MB is a function of the irradiation time for different samples. Where ρ_0 is the initial concentration of MB solution, ρ is the concentration of MB solution under light irradiation with t min. After light irradiation with 180 min, the concentration retention of MB degraded by different samples (a, b, c, e, f, g, h and i) are 29%, 14%, 39%, 31%, 28%, 25%, 23% and 22%, respectively. Obviously, the sample b (pH=6, heating temperature is 180°C for 8 h) is with the best photocatalytic activity, which is attributed to its wider bandgap.

In the heterogeneous catalytic reaction with plenty reactant, if the density of activity center on the catalyst surface is constant, the catalyst with the bigger specific surface will have the greater activities[19]. The specific surface area of photocatalyst is an important factor to decide photocatalytic reaction caused via photoinduced electron-hole pairs on the surface of photo-catalyst[18]. Therefore, the peanuts-like $BiVO_4$ nanoparticles have better photocatalyst activities than ordinary particles due to obvious quantum size effect, large specific surface area and high diffusion rate of photo-generated carriers[4,19]. Moreover, the wider photo-absorption range and better crystallinity caused by calcination effect are also favorable for its enhanced photocatalytic activity, resulting in the excellent photocatalytic performance of $BiVO_4$.

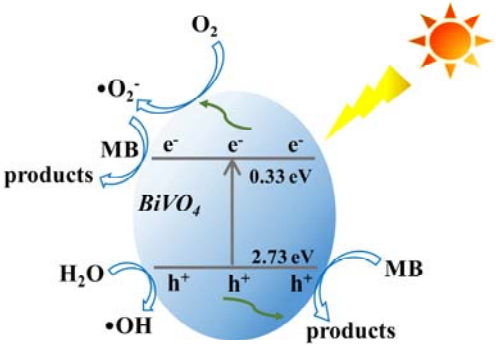

Figure 6. The schematic diagram of charge separation and photocatalytic process of the $BiVO_4$ photocatalysts under visible light irradiation.

Based on the reactive species trapping experiment results, a proposed mechanism for MB photocatalytic degradation by $BiVO_4$ photocatalysts is shown in **Figure 6**. The band gap of $BiVO_4$ is 2.4 eV[45]. Under visible light irradiation, the photo-generated electrons are occurred in the conduction band of the $BiVO_4$, photoinduced holes (h^+) are generated by the photoinduced transfer of electrons (e^-) in the $BiVO_4$, leading to an effective separation of the photo-generated electron-hole pairs. Along with the separated electrons and holes, the e^- are scavenged by oxygen to form $\bullet O_2^-$ radicals, which can degrade MB effectively. Meanwhile, most of the h^+ can oxidize MB to its degradation products directly, and little further contact with H_2O to produce hydro- xyl (•OH) radicals.

4. Conclusion

$BiVO_4$ has been synthesized successfully under different reaction conditions. And the fabricated $BiVO_4$ is the mixture of tetragonal and monoclinic $BiVO_4$ with different mix proportion. By adjusting the preparation conditions, the $BiVO_4$ phase changed from monoclinic phase to tetragonal phased. After high temperature annealing, the tetragonal phase all convert into the monoclinic phase. However, the different reaction conditions still affect the particles size and specific surface area of $BiVO_4$ samples. Moreover, it can be found that the photo-catalytic activities can be decided by the particles size and specific surface area of the samples.

Acknowledgments

This work was financially supported by National Natural Science Foundation of China (Grant No. 61376011), the National Science Foundation for Fostering Talents in Basic Research of the National Natural Science Foundation of China (Nos. 041105 and 041106), and the Fundamental Research Funds for the Central Universities (No. lzujbky-2017-k21).

References

1. Wang Y, Wang W, Mao H, *et al.* Electrostatic self-assembly of $BiVO_4$-reduced graphene oxide nano-

composites for highly efficient visible light photocatalytic activities. ACS Applied Materials & Inter faces 2014; 6(15): 12698–706.
2. Gu S, Li W, Wang F, *et al.* Synthesis of buckhorn-like $BiVO_4$ with a shell of CeOx nanodots: Effect of heterojunction structure on the enhancement of photocatalytic activity. Applied Catalysis B Environmental 2015; 170-171: 186–194.
3. Thalluri SM, Hernandez S, Bensaid S, *et al.* Green-synthesized W- and Mo-doped $BiVO_4$ oriented along the {0 4 0 facet with enhanced activity for the sun-driven water oxidation. Applied Catalysis B: Environmental 2016; 180: 630–636.
4. Gao X, Xu H, Yu J, *et al*. Controlled synthesis of $BiVO_4$ submicrospheres and their photocatalytic properties. Chemistry Letters 2015: 44(8): 1098–1100.
5. Li J, Cui M, Guo Z, *et al.* Synthesis of dumbbell-like CuO–$BiVO_4$ heterogeneous nanostructures with enhanced visible-light photocatalytic activity. Materials Letters 2014; 130: 36–39.
6. Ohno T, Akiyoshi M, Umebayashi T, *et al.* Preparation of S-doped TiO_2 photocatalysts and their photocatalytic activities under visible light. Applied Catalysis A: General 2004; 265(1): 115–121.
7. Zhang Y, Ma Q, Gao L, *et al.* Preparation and photoelectrochemical properties of nitrogen doped nanotubular TiO_2 arrays. Applied Surface Science 2013; 282: 174–180.
8. Shih YJ, Su CC, Chen CW, *et al.* Synthesis of magnetically recoverable ferrite (MFe_2O_4, M double bond Co, Ni and Fe)-supported TiO_2 photocatalysts for decolorization of methylene blue. Catalysis Communications 2015; 72: 127–132.
9. Ye J, Liu W, Cai J, *et al.* Nanoporous anatase TiO_2 mesocrystals: Additive-free synthesis, remarkable crystalline-phase stability, and improved lithium insertion behavior. Journal of the American Chemical Society 2011; 133(4): 933–940.
10. An H, Zhu B, Li J, *et al.* Synthesis and characterization of thermally stable nanotubular TiO_2 and itsphotocatalytic activity. The Journal of Physical Chemistry C 2008; 112(48): 18772–18775.
11. Tang Y, Wee P, Lai Y, *et al.* Hierarchical TiO_2 nanoflakes and nanoparticles hybrid structure for improved photocatalytic activity. The Journal of Physical Chemistry C 2012; 116(4): 2772–2780.
12. Asahi RT, Morikawa T, Ohwaki T, *et al*. Visible-light photocatalysis in nitrogen-doped titanium oxides. Science 2001; 293(5528): 269–271.
13. Khan SUM, Al-Shahry M, Ingler WB. Efficient photochemical water splitting by a chemically modified n-TiO_2. Science 2002; 297(5590): 2243–2245.
14. Putnam RL, Nakagawa N, Mcgrath KM, *et al*. Titanium dioxide−surfactant mesophases and Ti-TMS1. Chemistry of Materials 1997; 9(12): 2690–2693.
15. Brezova V, Blazkova A, Karpinsky L, *et al.* Phenol decomposition using M^{n+}/TiO_2 photocatalysts supported by the sol–gel technique on glass fibers. Journal of Photochemistry and Photobiology A: Chemistry 1997; 109(2): 177–183.
16. Bakar SA, Ribeiro C. Rapid and morphology controlled synthesis of anionic S-doped TiO_2 photocatalysts for the visible-light-driven photodegradation of organic pollutants. RSC Advances 2016; 6(43): 36516–36527.
17. Sakthivel S, Kisch H. Daylight photocatalysis by carbon-modified titanium dioxide. Angewandte Chemie International Edition 2003; 42(40): 4908–11.
18. Dong S, Feng J, Li Y, *et al.* Shape-controlled synthesis of $BiVO_4$ hierarchical structures with unique natural-sunlight-driven photocatalytic activity. Applied Catalysis B Environmental 2014; 152-153: 413–424.
19. Luo Y, Tan G, Dong G, *et al.* Effects of structure, morphology, and up-conversion on Nd-doped $BiVO_4$ system with high photocatalytic activity. Ceramics International 2015; 41(2): 3259–3268.
20. Ju P, Wang P, Li B, *et al.* A novel calcined Bi_2WO_6/$BiVO_4$ heterojunction photocatalyst with highly enhanced photocatalytic activity. Chemical Engineering Journal 2014; 236: 430–437.
21. Shi W, Yan Y, Yan X, *et al.* Microwave-assisted synthesis of nano-scale $BiVO_4$ photocatalysts and their excellent visible-light-driven photocatalytic activity for the degradation of ciprofloxacin. Chemical Engineering Journal 2013; 215-216: 740–746.
22. Guo M, He Q, Wang A, *et al.* A novel, simple and green way to fabricate $BiVO_4$ with excellent photocatalytic activity and its methylene blue decomposition mechanism. Crystals 2016; 6(7): 81.
23. Zhang X, Ai Z, Jia F, *et al.* Selective synthesis and visible-light photocatalytic activities of $BiVO_4$ with different crystalline phases. Materials Chemistry and Physics 2007; 103(1): 162–167.
24. Kudo A, Omori K, Kato H. A novel aqueous process for preparation of crystal form-controlled and highly crystalline $BiVO_4$ powder from layered vanadates at room temperature and its photocatalytic and photophysical properties. Journal of the American Chemical Society 1999; 121(49): 11459–67.
25. Chen H, Hu J, Xu B. Facile solid state method route synthesis and enhance visible light activities of $BiVO_4$ by doping Co. Key Engineering Materials 2016; 703: 316–320.
26. Tokunaga S, Kato H, Kudo A. Selective preparation of monoclinic and tetragonal $BiVO_4$ with scheelite structure and their photocatalytic properties. Chemistry of Materials 2001; 13(12): 4624–4628.
27. Li Y, Dong S, Wang Y, *et al.* Reduced graphene oxide on a dumbbell-shaped $BiVO_4$ photocatalyst for an augmented natural sunlight photocatalytic activity. Journal of Molecular Catalysis A Chemical 2014; 387: 138–146.
28. Peng F, Ni Y, Zhou Q, *et al.* Construction of ZnO nanosheet arrays within $BiVO_4$ particles on a conduc-

tive magnetically driven cilia film with enhanced visible photocatalytic activity. Journal of Alloys and Compounds 2017; 690: 953–960.
29. Yu C, Dong S, Feng J, *et al.* Controlled synthesis of uniform $BiVO_4$ microcolumns and advanced visible-light-driven photocatalytic activity for the degradation of metronidazole-contained wastewater. Environmental Science and Pollution Research International 2014; 21(4): 2837–2845.
30. Geng Y, Zhang P, Li N, *et al.* Synthesis of Co doped $BiVO_4$ with enhanced visible-light photocatalytic activities. Journal of Alloys and Compounds 2015; 651: 744–748.
31. Li J, Guo Z, Liu H, *et al.* Two-step hydrothermal process for synthesis of F-doped $BiVO_4$ spheres with enhanced photocatalytic activity. Journal of Alloys and Compounds 2013; 581: 40–45.
32. He Z, Shi Y, Chao G, *et al.* $BiOCl/BiVO_4$ p–n heterojunction with enhanced photocatalytic activity under visible-light irradiation. Journal of Physical Chemistry C, 2014, 118(1): 389–398.
33. Li R, Han H, Zhang F, *et al.* Highly efficient photocatalysts constructed by rational assembly of dual-cocatalysts separately on different facets of $BiVO_4$. Energy & Environmental Science, 2014, 7(4): 1369.
34. Song L, Pang Y, Zheng Y, *et al.* Design, preparation and enhanced photocatalytic activity of porous $BiOCl/BiVO_4$ microspheres via a coprecipitation-hydrothermal method. Journal of Alloys and Compounds 2017; 710: 375–382.
35. Zhou L, Wang W, Liu S, *et al.* A sonochemical route to visible-light-driven high-activity $BiVO_4$ photocatalyst. Journal of Molecular Catalysis A: Chemical 2006; 252(1-2): 120–124.
36. Jun YW, Choi JS, Cheon J. Shape control of semiconductor and metal oxide nanocrystals through nonhydrolytic colloidal routes. Angewandte Chemie (International ed. in English) 2006; 45(21): 3414–3439.
37. Yu J, Kudo A. Effects of structural variation on the photocatalytic performance of hydrothermally synthesized $BiVO_4$. Advanced Functional Materials 2006; 16(16): 2163–2169.
38. Yu J, Kudo A. Hydrothermal synthesis and photocatalytic property of 2-dimensional bismuth molybdate nanoplates. Chemistry Letters 2005; 34(11): 1528–1529.
39. Liu J, Wang H, Wang S, *et al.* Hydrothermal preparation of $BiVO_4$ powders. Materials Science and Engineering: B 2003; 104(1-2): 36–39.
40. Li Z, Chen D, Jiao X. Monoclinic structured $BiVO_4$ nanosheets: Hydrothermal preparation, formation mechanism, and coloristic and photocatalytic properties. The Journal of Physical Chemistry. B 2006; 110(6): 2668–73.
41. Dong S, Yu C, Li Y, *et al.* Controlled synthesis of T-shaped $BiVO_4$ and enhanced visible light responsive photocatalytic activity. Journal of Solid State Chemistry 2014; 211(5): 176–183.
42. Wetchakun N, Chaiwichain S, Inceesungvorn B, *et al.* $BiVO_4/CeO_2$ nanocomposites with high visible-light-induced photocatalytic activity. ACS Applied Materials & Interfaces 2012; 4(7): 3718–3723.
43. Guo Y, Xia Y, Ma F, *et al.* Additive-free controllable fabrication of bismuth vanadates and their photocatalytic activity toward dye degradation. Applied Surface Science 2010; 256(7): 2215–2222.
44. Zhang A, Zhang J, Cui N, *et al.* Effects of pH on hydrothermal synthesis and characterization of visible-light-driven $BiVO_4$ photocatalyst. Molecular Catalysis 2009; 304(1): 28–32.
45. Xu X, Zou Q, Yuan Y, *et al.* Preparation of $BiVO_4$-graphene nanocomposites and their photocatalytic activity. Journal of Nanomaterials 2014; 2014: 1–6.

Characterization and Application of Nanomaterials (2020) Volume 3 Issue 1
doi:10.24294/can.v3i1.716

ORIGINAL RESEARCH ARTICLE

Effect of multiple laser shock processing on nano-scale microstructure of an aluminum alloy

Simge Gencalp Irizalp*, Nursen Saklakoglu

Department of Mechanical Engineering, Celal Bayar University, Manisa Daire 45030, Muradiye, Turkey. E-mail: simge.gencalp@cbu.edu.tr

ABSTRACT

In this study, nano-scale microstructural evolution in 6061-T6 alloy after laser shock processing (LSP) was studied. 6061-T6 alloy plate was subjected to multiple LSP. The LSP treated area was characterized by X-ray diffraction and the microstructure of the samples was analyzed by transmission electron microscopy. Focused Ion Beam (FIB) tools were used to prepare TEM samples in precise areas. It was found that even though aluminum had high stacking fault energy, LSP yielded to formation of ultrafine grains and deformation faults such as dislocation cells, stacking faults. The stacking fault probability (PSF) was obtained in LSP-treated alloy using X-Ray diffraction. Deformation induced stacking faults lead to the peak position shifts, broadening and asymmetry of diffraction. XRD analysis and TEM observations revealed significant densities of stacking faults in LSP-treated 6061-T6 alloy. And mechanical properties of LSP-treated alloy were also determined to understand the hardening behavior with high concentration of structural defects.

Keywords: Laser Shock Processing; Microstructure; Deformation; Stacking Fault

ARTICLE INFO

Article history:
Received March 6 2020
Received in revised form 1 April 2020
Accepted 5 April 2020
Available online 21 April 2020

1. Introduction

Laser shock processing (LSP) is an innovative surface enhancement technique which has been used generally to improve mechanical performance of metallic components. LSP is a method of imparting compressive residual stress under laser shock amplitude loading[1]. Fatigue strength and fatigue life of a metallic material can significantly increase due to the presence of compressive residual stress in the material[2,3]. Also, the generated shock wave can induce severe plastic deformation in the specimen where the shock wave is effective[4,5]. The increase in hardness and yield strength of metallic materials is attributed to high-density dislocation arrays and the formation of twins owing to the shock wave[6-8]. Consequently, high-density dislocations and grain refinement mechanisms are induced in the laser-shocked near-surface microstructure of the metal.

Al-Mg-Si alloys are desirable in aerospace, automotive and shipping industries. Specifically, the 6061-T6 alloy has found widespread application due to a combination of high mechanical strength, low density, and good corrosion resistance[9,10]. It has been reported that compressive residual stress has been observed in 6061-T6 alloy samples under high-strain rate and ultra-high pressure, resulting in considerably improved tribological, fatigue and mechanical properties[5,10-14]. Recently, characterization studies at the nano-scale have become crucial in analyzing the microstructure induced by LSP. The mechanism

for microstructure evolution has a great importance in determining mechanical characteristics, because changes in mechanical characteristics can be understood in regard to microstructure. The sub-structures which create details of the microstructure are influenced by dynamic responses of the material due to shock stress loading[15]. Forming a nano-structure in a polycrystal results in the generation of dislocations, sub-grain structures, dislocation cells and stacking faults (SFs). In severe plastic deformation, the dislocation activity and stacking fault formation mechanism depends on the lattice structure and stacking fault energy probability (P_{SF})[9,16,17]. Chen *et al.*[18] found twin grains with SFs and breaking of large grains into smaller grains in the laser shocked area of 2Cr13Mn9Ni4 austenitic stainless steel. Ye *et al.*[19] found that dislocations were the dominant deformation modes in laser shocked copper foil and they propounded that SFE plays an important role in plastic deformation under conditions of ultrahigh strain rate. He *et al.*[6] noted that high density dislocation lines developed in the original grains caused by the shock wave at high strain rate during LSP.

However, most of the research was concentrated on the residual stress distribution versus depth and fatigue properties in components induced by LSP. The dynamic material response under compressive shock loading has a key role in terms of microstructural features. Microstructural changes at the nano-scale, the mechanism of grain refinement, and the underlying reasons for them have been discussed in previously mentioned reports in very few studies.

The aim of the present study is to investigate nano-scale characterization of LSP-treated materials using transmission electron microscopy (TEM). The grain refinement process under plastic deformation is revealed by considering the SFE of the material. In this regard, deformation mechanisms of LSP-treated materials, such as stacking faults, dislocation configuration and ultrafine grain formation, are investigated. Therefore, in this study, the strengthening mechanism was analyzed quantitatively by X-ray line profile analysis method and supported by TEM observations.

2. Experimental procedures

2.1 Principle and experimental procedure of LSP

The LSP parameters were typically selected to achieve a high power density[21]. Laser power density obtained in our previous experiments[5] was about 16.025 GW/cm^2. The laser pulse was directed through the transparent overlay and interacted with the opaque overlay and a plasma generated on the target material. The opaque overlay protected the sample surface from the thermal effect. The plasma was confined by the transparent overlay which was called “confined ablation”[3,11]. The hydrodynamic expanded plasma in the confined medium between the target material and the confining layer generates a high-pressure pulse. Therefore, a shockwave propagates into the material and the confining medium. When the magnitude of the shock wave exceeds the dynamic yield strength of the metal, plastic deformation occurs in the near surface of the metal[3,4,21]. Plastic deformation modifies the microstructure of specimen in the region affected from shock wave.

2.2 Experimental material and processing parameters

6061-T6 alloy was used in the present work. The thickness of material was 2 mm. The chemical composition of 6061-T6 alloy was shown in **Table 1**. Prior to LSP treatment, the samples were cleaned ultrasonically in ethanol to degrease their surfaces. And then, the specimens were covered with opaque black tape. They were immersed in a water of which the thickness above the target was 2 mm which is called confining medium. The LSP experiments were performed using a pulsed Nd:YAG laser operating at a repetition rate of 10 Hz, a wavelength of 1064 nm and a pulse duration of 6 ns. Laser beam spot diameter on the target was set to 1 mm. The overlapping rate was kept 50% between two laser-beam spots. The LSP procedure was performed in single LSP impact and double LSP impacts. The processing parameters used in LSP were shown in **Table 2**. During LSP, the target was operated in x and y-axis.

Table 1. Composition of 6061-T6 alloy

Si	Fe	Cu	Mn	Mg	Cr	Ni	Zn	Ti
0.62	0.46	0.29	0.09	0.88	0.17	0.01	0.04	0.05

Table 2. The processing parameters used in LSP

Type	Value
Pulse energy (mJ)	750
Spot size (mm)	1
Repetition rate (Hz)	10
Pulse duration (ns)	6
Laser wavelength (nm)	1064
Overlapping rate (%)	50

2.3 Microstructural observations

The microstructure of LSP-treated area of the samples was analyzed by transmission electron microscopy-TEM (FEI Tecnai G2 F30). The right observation within the material depended on significantly TEM specimen preparation technique. Focused Ion Beam (FIB) tools were used to prepare TEM samples in precise areas. The classical techniques for preparing TEM samples are not suitable for the analysis of a specific micrometric area in the specimen[22]. If the classical TEM samples preparation techniques were preferred, the dislocation densities and the dislocation evolution might alter in material microstructure. Therefore, this kind of process was avoided in particular in this work and so FIB was used as sample preparation method.

In TEM specimen preparation process, lift-out is a technique whereby membrane is produced in a thin sample, then cut free using the FIB and removed for stand-alone examination in the TEM. The procedure composes of four steps:

(1) A particular region was located by SEM. During milling which was subsequent step, to protect the investigated feature, platinum, tungsten or other weighty metal layer in order to protect it from deep damaging due to ion irradiation during milling was deposited on the area of interest.

(2) The material surrounding the platinum strip was removed by FIB milling and so a lamella which was performed on thin specimens transparent to electrons was left intact.

(3) A micromanipulator needle was fixed to the sample thanks to a platinum welding and then the lamella was cut free and lifted out of the milled cavity.

(4) The sample was placed in a TEM grid as so contact to the platinum weld, then the connection between lamella and needle was cut[22,23].

The samples of LSP-treated and un-treated were prepared by FIB/SEM (FEI Nova 600i Nano-lab) in attempt to analyze in depth 10 micron and they were made ready for TEM examinations.

2.4 X-Ray diffraction analysis

X-ray diffraction measurements were carried out using the Philips X'Pert Pro equipped with a Cu-Kα radiation source whose wavelength was 1.542Å. X-ray penetration depth is an order of 50μm. The broadening and position shifts of the full-width at half maximum (FWHM) of the α-Al {311} X-ray diffraction peak were considered to obtain the dislocation density, lattice strain, and stacking fault probability. The dislocation density values were obtained from our former study[21]. The lattice strain and the stacking fault probability measurement and calculation were realized on a certain plane in this study, the peaks of the α-Al (311) lattice plane is recommended in X-ray diffraction technique for aluminum alloys because this plane is the intense peak plane from X-ray diffraction data[24]. Lattice strain was calculated by Scherrer equation[25]. This procedure was reported well documented in our previous work[5]. The stacking fault energy γ is inversely proportional to stacking fault probability (P_{SF})[26] and the stacking fault probability was determined by following equation developed by Noskova and Pavlov[27]:

$$P_{SF} = \frac{G a_0^{\,2} d\rho}{24\pi\gamma}$$

Where the stacking fault energy γ consists of the contribution of the stacking fault probability P_{SF}, shear modulus G, lattice constant a_0, lattice space of determined crystal plane$d$, dislocation density ρ.

2.5 Measurements of micro-hardness and tensile properties

The hardness properties of LSP-impacted alloy were investigated by micro-hardness measurement using Vickers-indenter. The tests were

carried out under 50 g load and 10s of the hold time. The hardness measuring was performed on the metal surface. Tensile properties were determined using a Schimadzu testing machine and by a video extensometer. The tensile tests were carried out at a room temperature and a displacement rate 1 mm/min.

3. Results and discussion

Micrographs obtained from TEM examinations, which were performed to investigate the LSP-treated and un-treated 6061-T6 alloy prepared by the FIB technique, are given below.

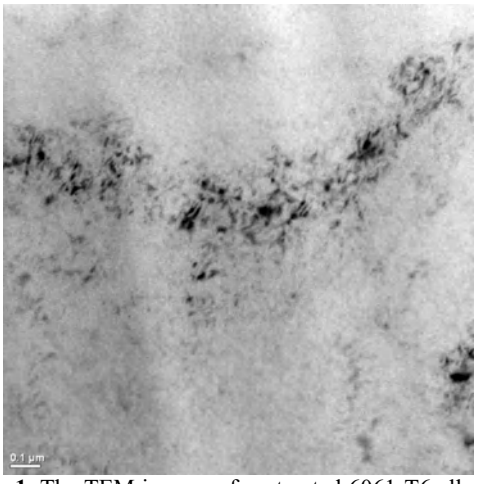

Figure 1. The TEM images of un-treated 6061-T6 alloy: low dense dislocation line**.**

The TEM images of untreated alloy are shown in **Figure 1**. Low-density dislocations are clearly seen. There are low density defects in the microstructure. **Figure 2** shows TEM images which were obtained from single LSP impact. LSP created stacking faults (SF) can be seen in (**Figure 2**). SF is a defect type which affects the mechanical properties of crystalline materials and is commonly seen in materials with low stacking fault energy (SFE)[28]. SFs can be formed during crystal growth, due to acts of partial dislocations during plastic deformation or as a result of separation of total dislocations into two partial dislocations. The dislocation separation distance is related to the magnitude of the SFE. SFs can also be generated by the excess point defects produced in severe plastic deformation or high-strain rate deformation or laser irradiation[28].

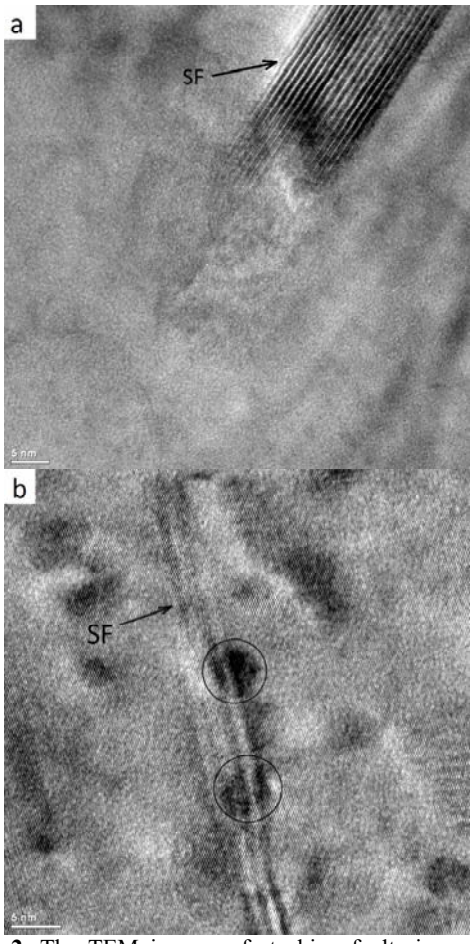

Figure 2. The TEM images of stacking faults in one-LSP impact alloy **(a)** and **(b).**

SFs are local regions of incorrect sequence of crystal planes associated with the presence of partial dislocations. SFs originate from dissociation of dislocations to reduce the elastic energy of the crystal[29]. If the local region formed as a result an incorrect sequence is of a few interatomic distances, it is called a “stacking fault”, and if it is of numerous interatomic distances, it is called “twinning”. While twinning is a dominant deformation mechanism in materials with low-SFE (e.g. copper, brass), it can be rarely formed in materials with high-SFE such as aluminum. Laser shock processing can create a large amount of SFs in 6061-T6 aluminum alloy due to ultra-high plastic strain. In **Figure 2(b)**, multiple dislocation cores interact with the SFs. The indicated regions in **Figure 2(b)**, which are shaped like dark circles, are trapped dislocations. The trapped dislocations indicated with circles intercept the SF plane.

When **Figure 3** was observed, it was seen that the dislocations were organized and these well-organized dislocations created the dislocation

cell walls. Ren *et al.*[30] observed band-like dislocation walls in TEM observations which performed in LSP GH2036 and they reported that the dislocation walls coincident with slip planes. When **Figure 3(a)** and **3(b)** were examined, the dislocation walls having tangled dislocation boundaries attracted the attention in the single LSP impacted 6061-T6 alloy and also looked band-like. The dislocation cell formation notably reduces the stored energy in deformed crystallites[31]. For this reason, the high energy induced by the LSP into the material tends to create dislocation cells.

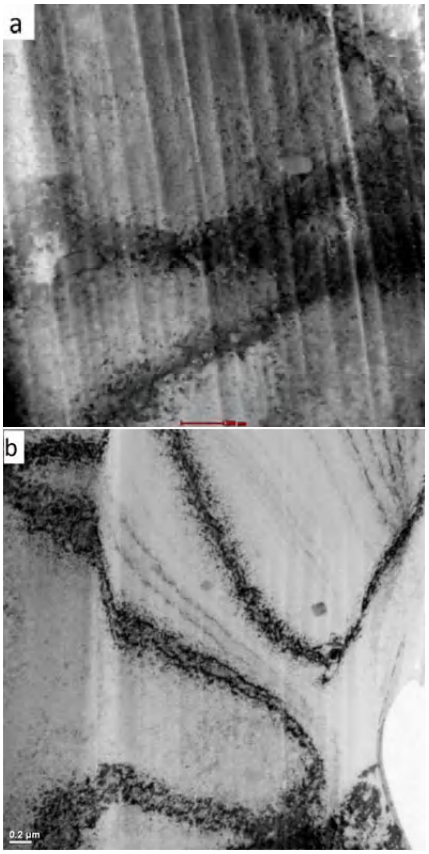

Figure 3. The TEM images of the well-organized dislocation cell walls and subgrain structures.

It was observed that dislocation tangled zones occurred and heavily deformed subgrain structures derived from dislocation cell structures induced in laser shock processing. Shin *et al.*[32] stated that cell boundary can originate from severely tangled dislocations and therefore subgrains induced. It was seen that the subgrains of which size is about 300-800 nm in **Figure 3(a)**. And also, when the cell structure was observed, it was realized that the high density dislocations existed at the boundary but the low density dislocations observed inside. The severe plastic deformation induced by LSP caused the dislocation piping and induced heavily tangled dislocation lines and consequently, dense dislocation walls occurred. The white lines which are seen in **Figure 3** are certain effect and originated from FIB preparation process.

Lu *et al.*[33], Wang *et al.*[34] and Liu *et al.*[35] argued that the subgrain boundaries developed by dislocation transformation. It is known that the stacking faults formed among partial dislocations in FCC metals[36]. Sun *et al.*[37] stated that there were two factors governing the grain refinement: stacking fault energy and slip system numbers. Lu *et al.*[38] remarked that the dislocation cell formation in the metals which have medium SFE results in grain refinement. In high SFE metals, dislocation walls and tangles formation leads to the refinement mechanism but SF formation is difficult. In consequence, plastic deformation behavior of the materials depends strongly on the SFE[38]. During severe plastic deformation, the point defections and SFs in the crystal interact with each other and new atoms move on SF region. Therefore, new atoms located and grouped in the SF and so stacking fault energy is decreased, and partial dislocations were opened and resulted in stacking fault ribbon widening[36].

The deformation microstructure of face-centered cubic materials is complex. Many grains in face-centered cubic materials have sharp grain boundaries and non-uniform sized grains[35]. It was also seen that organized dislocations and dislocation cells formed in **Figure 4**. Dislocation cells corresponded to sub-grain formation in the TEM investigations. Growth of cellular microstructure is formed by separation from organized dislocations[39]. The term “cell” usually refers to small volumes formed by diffuse dislocation boundaries, and also the term“subgrain” refers to bounding more organized dislocations. Dislocation cells which organized after deformation correspond to the “subgrain”. Comparing with untreated alloy, it is obvious that the dislocation arrangements in the networks become more complex and tangled. High-density dislocation lines, a dislocation network and a dislocation wall which

corresponds to a sub-grain boundary can be clearly seen in one-impact LSP. Stacking faults can be formed by the homogenous mechanism enhancing the possibilities of the material to respond to dynamic loading. Severe plastic deformation formed obvious stacking faults while aluminum has high SFE.

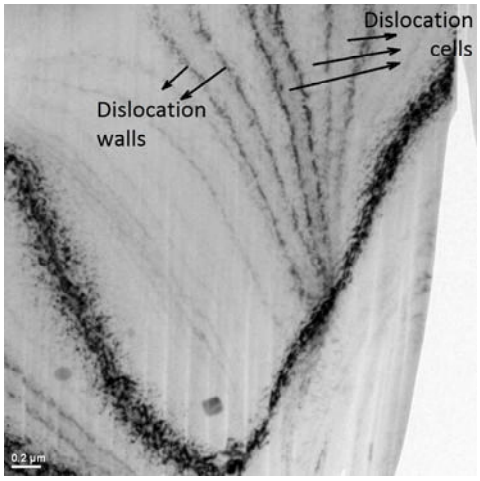

Figure 4. The TEM images of the organized dislocation and dislocation cells in single LSP impact alloy**.**

The TEM images of double-LSP impact alloy were given in **Figure 5**. Nano grain with size of 40-50 nm which contains trapped dislocations (white arrows) is seen in **Figure 5(a)** and **Figure 5(b)** shows both ultrafine grains with size of 200-300 nm and nano-grain having size of about 50 nm. This TEM image showed that ultrafine grains can be deformed by dislocation motion. The ultra-fine grains and nano-grains have darker contrast in comparison to micro-sized grains. Because the ultrafine size leads to randomly oriented grains, therefore, allows the variations in dynamical diffracting conditions[31,40]. The ultrafine grains contain high internal stress and this situation gets elastic distortions in crystal lattice[31]. Higher density dislocation regions especially induced by severe plastic deformation are in accordance with higher mis-orientations. The subgrain boundaries disturb the deformation coordination and higher density dislocations accumulated and rearranged, thus, lower angle subgrain boundaries induced by plastic strain increasing. Finally, finer grains are formed[41].

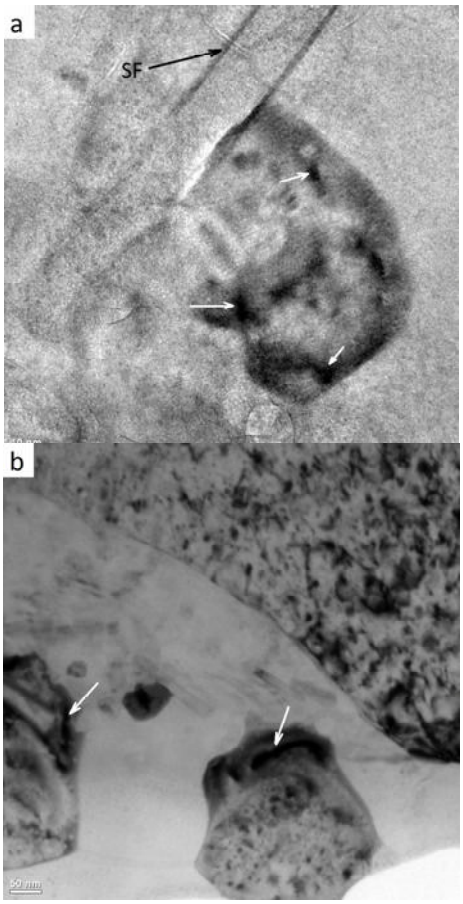

Figure 5. TEM micrograph of trapped dislocations in a nano-grain: **(a)** nano-grains and ultrafine grains, **(b)** in double LSP impact alloy**.**

After double LSP impact, rearrangement of dislocations occurs and leads to newly ultrafine grains. Local distortions in terms of trapped dislocations are clearly visible in the TEM micrograph. The main cause for the locally distributed/trapped dislocations is associated with the energy stored during plastic deformation at nano-scale in the lattice structure[42]. Therefore, the short duration of plastic deformation under the localized load is responsible for the dislocation trapping in the nano-scale structure. The development of the dislocations during LSP process was clearly seen in **Figure 6**. Low-density dislocations in high magnification attract the attention for un-treated alloy in **Figure 6(a)**. Tangled and dense dislocation arrangements were seen in the laser shocked region (**Figure 6(b)** and **(c)**).

Comparing the microstructures, the one-LSP impact treated specimen presents some dislocations which have discrete structure and are small in length and the double LSP impact treated specimen presents the distinctively different char-

acteristics which are longer and more complex in shape and it has dislocation nodes.

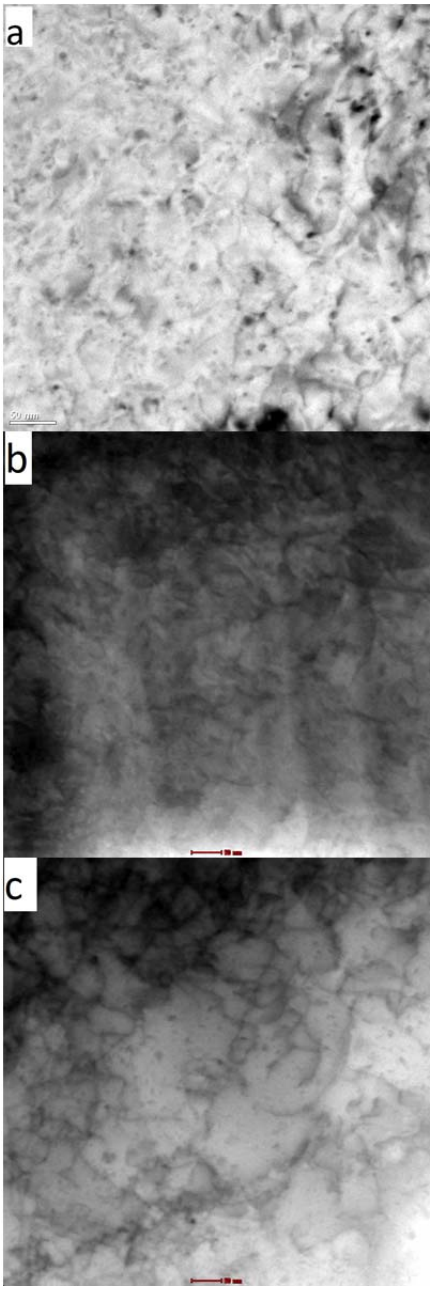

Figure 6. TEM image of dislocations : **(a)** un-treated alloy, **(b)** single-LSP impacted alloy, **(c)** double LSP-impacted alloy**.**

The tangled dislocations were also observed to dissociate into partial dislocations. Chen *et al.*[43] found that the deformation generated adjacent local areas with different orientations when the metal was exposed to plastic deformation. In consequence of laser shock processing, crystallites which had low-angle orientation boundaries were generated in the near-surface regions. Thus, nano-grains with different orientation were produced inns-pulsed laser experiments. Formation of nano-crystalline structures in aluminum alloy after laser shock processing broadly was investigated by X-ray line profile analysis in our previous work[21].

Figure 7 shows the diffraction peak profiles of (311) for untreated, single LSP impacted and double LSP impacted alloy and this diffraction profiles were received from our previous work[21]. Peak broadening and shifts are clear as a result of laser shock processing. Line broadening analysis of XRD peaks explores the crystallite size which for samples with lattice faults[21]. Moreover, the peak broadening analysis was also used to determine the stacking fault probability (P_{SF})[44-46]. The peak shift and broadening were affected from randomly oriented crystallites with small faulting probabilities[44]. The Bragg's law and equation (1) were used for calculations and the values of d-spacing, stacking fault probability and lattice strain for all the samples were listed in **Table 3**. The values of dislocation density in **Table 3** received from our previous work[21]. The deformed material during laser shock processing, and the non-uniform strain happened in the crystal lattice led to a broadening in FWHM of X-ray diffraction peak. The lattice strain is defined as the increment of inter-planar spacing and as a function of the exposed strain[44]. Moreover, lattice strain can be expressed as micro-strain of the lattice deformation[47]. According to **Figure 7**, lattice strains considerably affected the diffraction peak profiles as a broadening in FWHM after LSP. As it is known, high strain rate deformation causes lattice distortion and work hardening. Lattice distortion brings the dislocations and new grain boundaries[48].

In low SFE materials, stacking faults and twin formation play an important role in the formation of nanostructures and ultrafine grains[49-52]. Coarse grained FCC metals with high stacking fault energy such as aluminum is anticipated to deform by dislocation slip. However, when the material was deformed in high strain rate deformation condition, the stacking fault and twin formation conditions have improved. At the same time, the high strain rate deformation condition contributed to nano-crystalline formation. Shock deformation has been found to produce twins and

stacking faults in medium-high stacking fault energy alloys[53].

Table 3. X-ray line profile analysis results of 6061-T6 alloy

	2θ of (311) plane[21]	Dislocation density, $\rho_{dis}\rho_{dis}$ (10^{14} lines/m^2)[21]	Lattice strain,ε	d-spacing (nm)	Stacking fault probability, P_{SF}
Un-treated	78.166	7.367	0.089	0.78774	0.02183
Single LSP impact	78.100	18.437	0.141	0.78793	5.4668
Double LSP impact	78.034	19.092	0.143	0.78812	5.6624

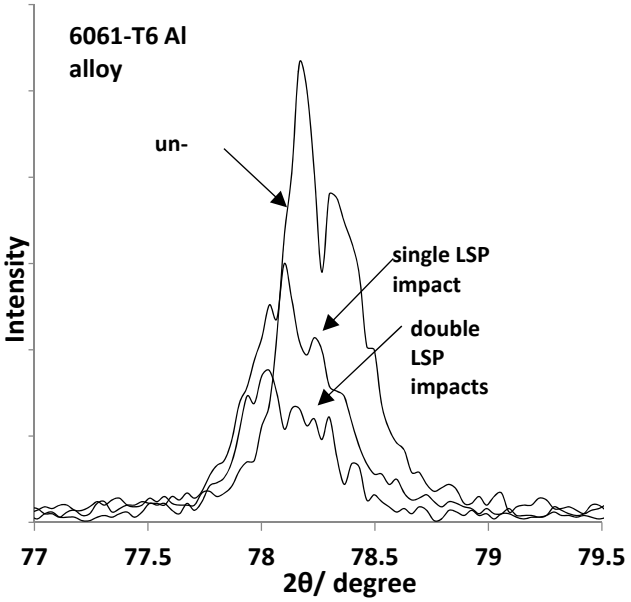

Figure 7. X-ray diffraction patterns (311) of 6061-T6 alloy subjected to various LSP impacts[21].

Atultra-high strain rate, the energy required for the motion of a perfect dislocation is higher than that required for the motion of two partial dislocations formed by the decomposition of a perfect dislocation. As it is known, the formation of the stacking faults is inversely depended on the stacking fault energy. Therefore, low SFE and high stacking error probability lead to the formation of a large number of stacking errors[18]. Wert *et al.*[54] stated that the particle size decreased with decreasing SFE, while the stacking fault probability increased.

Figure 8 shows the variation in the stacking fault probability (P_{SF}), lattice strain (ε), and dislocation density (ρ_{dis}) as a function of process parameters. As shown in **Figure 8(a)**, the dislocation density was 7.367x10^{14} m^{-2} for the untreated alloy. The dislocation density value strongly increased via laser shock processing. It was reached the ρ_{dis} value of 19.092 x10^{14} m^{-2} with double shot LSP impact. **Figure 8(b)** shows the evolution of the lattice strain (ε) increased after LSP treatment. The increase in ε indicates that the severe lattice distortion introduced during LSP yielded tore-arrangement of dislocation. **Figure 8(c)** shows the evolution of the stacking fault probability (P_{SF}) increased after LSP treatment.

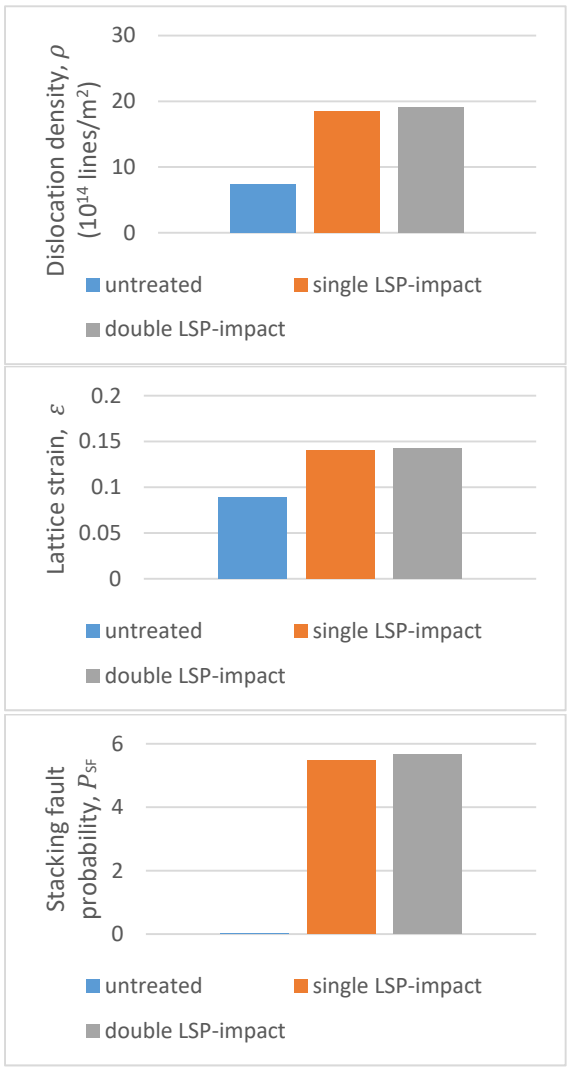

Figure 8. Plot showing the variation of **(a)** dislocation density, **(b)** latticestrain, and **(c)** stacking fault probability with process parameter for 6061-T6 alloy**.**

The stacking fault probability was also obtained from the peak asymmetry of (311) Bragg's peak. The stacking fault probability in 6061-T6 alloy increased sharply with LSP treatment. Thus, the increase in stacking fault probability in 6061-T6 alloy will decreased the SFE after high strain rate deformation[55-56].

There are five main strengthening mechanism in the metallic materials: solid-solution hardening, precipitation hardening, transformation hardening, dislocation hardening and grain refinement[57-58]. The solid-solution hardening and precipitation hardening did not significantly affect the strength of the exposed specimen. The dislocation hardening and grain refinement brings a significant increase in the materials strength. When the stress applied to the material exceeds the yield strength, perfect dislocations both move and multiply. In alloys with low stacking fault energy, a perfect dislocation dissociates into two dislocations and two extended dislocations form. When two extended dislocations on the conjugate slip planes intersect each other, extended jogs and Cottrell ± Lomer locks are formed. They prevent the movement of dislocations and so an increase in the strain hardening occurs. The lower the SFE is, the higher the stacking fault probability is, and the wider the stacking fault ribbons is, resulting in more difficult cross slip, increased strain hardening and prolonged linear hardening stage[59].

Table 4. Mechanical properties of LSP impacted 6061-T6 alloy

Parameters	Surface hardness ($HV_{0.05}$)	UTS (MPa)	YS (MPa)
Untreated	97	214	177
Single LSP-impact	113	316	280
Double LSP-impact	121	312	286

Examinations of the mechanical properties have indicated work hardening behavior of LSP impacted materials. When **Table 4** examined, mechanical properties have been improved effectively by LSP. After single LSP-impact, its surface hardness improved from 97 $HV_{0.05}$ to 113 $HV_{0.05}$ and after double LSP impact, improved to 121 $HV_{0.05}$. And also, after LSP treatment, UTS approximately increased 45%, and YS increased 60%. The mechanical properties of LSP after impact are not only due to the increase of stacking fault probability, but also due to the significant increase of dislocation density and lattice strain. High density dislocation arrangement and also new ultrafine grain structure reveal the strengthening mechanism. But in this study, it is not enough to explain the behavior of strengthening with only grain refinement and high density dislocation. In the high strain rate process, LSP treatment increases PSF value (**Figure 8(c)**). The dramatic increase in stacking fault probability has triggered the formation of stacking faults. High P_{SF} is associated with a decrease in stacking fault energy. As it is known, partial dislocations were opened with SFE decreasing and the SFE formation was launched by the interaction between partial dislocations and point defections. The SFE of FCC metal was decreased, and the dislocation accumulation and stacking accumulation were decreased, and the work hardening behavior was improved[38]. The dislocation accumulation, accumulated SFs and ultrafine grain structure provided the extra strengthening. These inferences are in good agreement with TEM observations. XRD line analysis is an effective method for the determination of SF, grain size, lattice strain and dislocation density[5,57,60]. The SF strengthening, nanostructure and ultrafine grained microstructure were obtained after severe plastic deformation (SPD), equal channel angular pressing (ECAP), and high-pressure torsion (HPT)[61-64]. In this study, sheet metal samples were exposed to high strain rate by LSP method which is applied to the industry and a significant strengthening behavior was induced by microstructural development of the material.

Figure 9 shows the stacking faults in atomic resolution. Liao *et al.* and Lee *et al.*[65-66] reported the typical stacking faults in atomic level image. The SF width in **Figure 9(a)** was about 0.4 nm and in **Figure 9(b)** was about 0.7 nm. It is seen that the double LSP impact is responsible for the wide SF. The lowering SF energy led to a wider stacking fault and higher stacking fault probability. SFs interact with point defections in the crystal. During the mechanical reaction in the material through several plastic deformations, new atoms move towards SF region and so elastic-energy of the crystal reduces. This formation occurring between the partial dislocations causes a reciprocal push of the partial dislocations, which lowers the SFE, so that a widening of the SF band can be observed[36]. Partial dislocations restricted by a stacking fault ribbon[66].

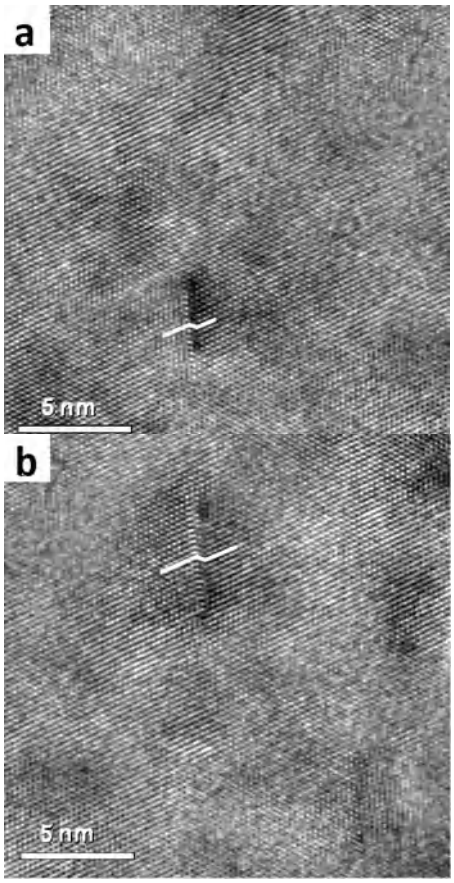

Figure 9. Atomic level image of a typical stacking faults after **(a)** single LSP impact and **(b)** double LSP impact**.**

In this study, stacking fault bands can be observed during laser shock treatment with high-strain rates, even if the material was a high SFE metal. Ye *et al.*[19] reported that dislocation slip was the dominant deformation mode at small-strain conditions. However, under shock conditions, stacking faults and twins were formed besides dislocation slip. In terms of microstructural observations, dislocation cells, and stacking faults subdivide the initial coarse grain into randomly ultra-refined grains. High-strain rate and a short duration laser pulse play an important role in the formation of refined grains during micro plastic deformation by LSP.

4. Conclusions

The aims of the present work were to investigate the formation of dislocations, dislocation cell structures, lattice orientations and sub-structures at the nano-scale under shock loading. TEM investigations demonstrated the formation of stacking faults, dislocation arrangements and ultrafine grains. Multiple LSP impacts at high-strain rate created more dislocations, which could generate stacking faults, nano-grain and ultrafine grain structures. The main results showed that the stacking fault probability significantly increased from 0.02183 to 5.6624 and dislocation density increased from 7.367 to 19.092 after LSP treatment. Microstructural parameters were also in good agreement with the results of X-ray line profile analysis. The short duration and high pressure effect of plastic deformation under the localized load lead to the trapping of dislocations in nano-scaled structures. The LSP results presented highly tangled and dense dislocations and dislocation cell-structures. It clearly showed the hardness increment in LSP treatment material. This increment resulted from grain refinement, dense dislocation structure and stacking faults. Experimental observations and evidence of the grain refinement mechanism demonstrated that a high-SFE metal which was deformed at high-strain rates could form ultrafine grains, and stacking faults.

Acknowledgments

The authors would like to thank Celal Bayar University (Project Code: 2012-009) for providing financial support. They would also like to thank for the financial support given to Laser Technologies Research and Application Center (LATARUM).

References

1. Ren X, Zhang Y, Zhang T, *et al.* Comparison of the simulation and experimental fatigue crack behaviors in the nanoseconds laser shocked aluminum alloy. Materials & Design 2011; 32(3): 1138–1143.
2. Yang C, Hodgson PD, Liu Q, *et al.* Geometrical effects on residual stresses in 7050-T7451 aluminum alloy rods subject to laser shock peening. Journal of Materials Processing Tech 2008; 201(1-3): 303–309.
3. Ye L, Ding K. Laser shock peening: Performance and process simulations. Cambridge: Woodhead Publishing; 2006. p. 172.
4. Lu J, Luo K, Zhang Y, *et al.* Grain refinement mechanism of multiple laser shock processing impacts on ANSI 304 stainless steel. Acta Materialia 2010; 58(16): 5354–5362.
5. Irizalp SG, Saklakoglu N, Yilbas BS. Characterization of microplastic deformation produced in 6061-T6 by using laser shock processing. Interna-

tional Journal of Advanced Manufacturing Technology 2014; 71(1-4): 109–115.
6. He T, Xiong Y, Guo Z, *et al.* Microstructure and hardness of laser shocked ultra-fine-grained aluminum. Journal of Materials Science & Technology 2011; 27(9): 793–796.
7. Chu JP, Rigsbee JM, Bana G, *et al.* Laser-shock processing effects on surface microstructure and mechanical properties of low carbon steel. Materials Science & Engineering A 1999; 260(1-2): 260–268.
8. Li Y, Zhou L, He W, *et al.* The strengthening mechanism of a nickel-based alloy after laser shock processing at high temperatures. Science & Technology of Advanced Materials 2013; 14(5): 1–9.
9. Ren X, Ruan L, Yuan S, *et al.* Dislocation polymorphism transformation of 6061-T651 aluminum alloy processed by laser shock processing: Effect of tempering at the elevated temperatures. Materials Science & Engineering 2013; 578: 96–102.
10. Sathyajith S, Kalainathan S, Swaroop S. Laser peening without coating on aluminum alloy Al-6061-T6 using low energy Nd: YAG laser. Optics & Laser Technology 2013; 45: 389–394.
11. Gencalp Irizalp S, Saklakoglu N, Akman E, *et al.* Pulsed Nd: YAG laser shock processing effects on mechanical properties of 6061-T6 alloy. Optics & Laser Technology 2014; 56: 273–277.
12. Rubio-Gonzalez C, Gomez-Rosas G, Ocana JL, *et al.* Effect of an absorbent overlay on the residual stress field induced by laser shock processing on aluminum samples. Applied Surface Science 2006; 252(18): 6201–6205.
13. Rubio-Gonzalez C, Ocana JL, Gomez-Rosas G, *et al.* Effect of laser shock processing on fatigue crack growth and fracture toughness of 6061-T6 aluminum alloy. Materials Science and Engineering: A 2004; 386(1-2): 291–295.
14. Sanchez-Santana U, Rubio-Gonzalez C, Gomez-Ro sas G, *et al.* Wear and friction of 6061-T6 aluminum alloy treated by laser shock processing. Wear 2006; 260(7-8): 847–854.
15. Kalantar DH, Belak J, Bringa E, *et al.* High-pressure, high-strain-rate lattice response of shocked materials. Physics of Plasmas 2003; 10(5): 1569–1576.
16. Cao XJ, Pyoun YS, Murakami R. Fatigue properties of a S45C steel subjected to ultrasonic nanocrystal surface modification. Applied Surface Science 2010; 256(21): 6297–6303.
17. Zehetbauer M, Valiev RZ. Nanomaterials by severe plastic deformation. Weinheim, Berlin: Wiley-VCH; 2004. p. 1–850.
18. Chen K, Zheng C, Yuan Z, *et al.* Deformation microstructures of austenitic stainless steel 2Cr13-Mn9Ni4 under ultrafast strain rate by laser shock processing. Materials Science and Engineering A: Structural Materials: Properties, Microstructure and Processing 2013; 587: 244–249.
19. Ye Y, Feng Y, Lian Z, *et al.* Plastic deformation mechanism of polycrystalline copper foil shocked with femtosecond laser. Applied Surface Science 2014; 309: 240–249.
20. Yilbas BS, Arif AFM, Shuja CZ, *et al.* Investigation into laser shock processing. Journal of Materials Engineering and Performance 2004; 13: 47–54.
21. Saklakoglu N, Gencalp Irizalp S, Akman E, *et al.* Near surface modification of aluminum alloy induced by laser shock processing. Optics & Laser Technology 2014; 64: 235–241.
22. Jublot M, Texier M. Sample preparation by focused ion beam micromachining for transmission electron microscopy imaging in front-view. Micron 2014; 56: 63–67.
23. Grassian VH (editor). Nanoscience and Nanotechnology. Bridgewater, New Jersey: John Wiley & Sons, Inc.; 2008. p. 461.
24. Committe AIH. Metals handbook volume 10 — Materials characterization. Fifth Printing. Novelty, Ohio: ASM Int; 1998. p. 1310.
25. Fultz B, Howe JM. Diffraction lineshapes. In: Transmission electron microscopy and diffractometry of materials. 4th ed. Berlin Heidelberg: Springer; 2013. p. 429–462.
26. Zhou W, Jiang B, Liu Y, *et al.* Stacking fault probability and stcaking fault energy in CoNi alloys. Transactions of Nonferrous Metals Society of China 2001; 11(4): 555–558.
27. Noskova NI, Pavlov VA. Stacking faults in nickel solid solutions. Physics Metal and Metallography 1962; 14: 86.
28. Li B, Yan P, Sui M, *et al.* Transmission electron microscopy study of stacking faults and their interaction with pyramidal dislocations in deformed Mg. Acta Materialia 2010; 58(1): 173–179.
29. Hull D, Bacon DJ. Introduction to dislocations. 3rd ed. Oxford, United Kingdom: Pergamon Press. 1984. p. 80.
30. Ren X, Zhou W, Ren Y, *et al.* Dislocation evolution and properties enhancement of GH2036 by laser shock processing: Dislocation dynamics simulation and experiment. Materials Science & Engineering: A 2016; 654: 184–192.
31. Xu Z, Liu M, Jia Z, *et al.* Effect of cryorolling on microstructure and mechanical properties of a peak-aged AA6082 extrusion. Journal of Alloys and Compounds 2017; 695: 827–840.
32. Shin DH, Park JJ, Kim YS, *et al.* Constrained groove pressing and its application to grain refinement of aluminum. Materials Science & Engineering: A 2002; 328(1-2): 98–103.
33. Lu J, Luo K, Zhang Y, *et al.* Grain refinement of LY2 aluminum alloy induced by ultra-high plastic strain during multiple laser shock processing impacts. Acta Materialia 2010; 58(11): 3984–3994.
34. Wang J, Zhang Y, Chen J, *et al.* Effect of laser sho- ck peening on the high-temperature fatigue performance of 7075 aluminum alloy. Materials Science & Engineering: A 2017; 704: 459–468.
35. Liu M, Roven HJ, Yu Y, *et al.* Deformation struc-

tures in 6082 aluminium alloy after severe plastic deformation by equal-channel angular pressing. Materials Science & Engineering: A 2008; 483-484: 59–63.
36. Gencalp Irizalp S, Saklakoglu N. High strength and high ductility behavior of 6061-T6 alloy after laser shock processing. Optics & Lasers in Engineering 2016; 77: 183–190.
37. Sun H, Shi Y, Zhang M, *et al.* Plastic strain-induced grain refinement in the nanometer scale in a Mg alloy. Acta Materialia 2007; 55(3): 975–982.
38. Lu K, Lu J. Nanostructured surface layer on metallic materials induced by surface mechanical attrition treatment. Materials Science & Engineering: A 2004; 375-377: 38–45.
39. Hurley PJ, Humphreys FJ. Modelling the recrystallization of single-phase aluminium. Acta Mater 2003; 51(13): 3779–3793.
40. Zhang X, Hu T, Rufner JF, *et al.* Metal/ceramic interface structures and segregation behavior in aluminum-based composites. Microscopy and Microanalysis 2015; 21(S3): 1053–1054.
41. Zhang Y, Jiang S. The mechanism of inhomogeneous grain refinement in a NiTiFe shape memory alloy subjected to single-pass equal-channel angular extrusion. Metals 2017; 7(10): 400.
42. Youssef KM, Scattergood RO, Murty KL, *et al.* Ultrahigh strength and high ductility of bulk nanocrystalline copper. Applied Physics Letters 2005; 87(9): 1–3.
43. Chen H, Yao YL, Kysar JW. Spatially resolved characterization of residual stress induced by micro scale laser shock peening. Journal of Manufacturing Science and Engineering 2004; 126 (2): 226–236.
44. Jeong JS, Woo W, Oh KH, *et al.* In situ neutron diffraction study of the microstructure and tensile deformation behavior in Al-added high manganese austenitic steels. Acta Materialia 2012; 60(5): 2290–2299.
45. Tomota Y, Tokuda H, Adachi Y, *et al.* Tensile behavior of TRIP-aided multi-phase steels studied by in situ neutron diffraction. Acta Materialia 2004; 52(20): 5737–5745.
46. Jeong JS, Koo YM, Jeong IK, *et al.* Micro-structural study of high-Mn TWIP steels using diffraction profile analysis. Materials Science & Engineering: A 2011; 530: 128–134.
47. Rafaja D, Sııma M, Klemm V, *et al.* X-ray diffraction on nanocrystalline $Ti_{1-x}Al_xN$ thin films. Journal of Alloys and Compounds 2004; 378(1-2): 107–111.
48. Nie X, He W, Zhou L, *et al.* Experiment investigation of laser shock peening on TC6 titanium alloy to improve high cycle fatigue performance. Materials Science & Engineering: A 2014; 594: 161–167.
49. Huang C, Hu W, Yang G, *et al.* The effect of stacking fault energy on equilibrium grain size and tensile properties of nanostructured copper and copper–aluminum alloys processed by equal channel angular pressing. Materials Science & Engineering: A 2012; 556: 638–647.
50. Das J. Evolution of nanostructure in α-brass upon cryorolling. Materials Science and Engineering: A 2011; 530: 675–679.
51. Roy B, Kumar NK, Nambissan PMG, *et al.* Evolution and interaction of twins, dislocations and stacking faults in rolled α-brass during nanostructuring at sub-zero temperature. AIP Advances 2014; 4(60): 1–8.
52. Kumar NK, Roy B, Das J. Effect of twin spacing, dislocation density and crystallite size on the strength of nanostructured α-brass. Journal of Alloys and Compounds 2015; 618: 139–145.
53. Zhu Y, Liao X, Wu X. Deformation twinning in nanocrystalline materials. Progress in Materials Science 2011; 57(1): 1–62.
54. Wert JJ, Singerman SA, Caldwell SG, *et al.* An X-ray diffraction study of the effect of stacking fault energy on the wear behavior of Cu-Al alloys. Wear 1983; 92(2): 213–229.
55. Talonen J, Hanninen H. Formation of shear bands and strain-induced martensite during plastic deformation of metastable austenitic stainless steels. Acta Materialia 2007; 55(18): 6108–6118.
56. Gong Y, Wen C, Wu X, *et al.* The influence of strain rate, deformation temperature and stacking fault energy on the mechanical properties of Cu alloys. Materials Science & Engineering: A 2013; 583: 199–204.
57. Yamanaka K, Mori M, Sato S, *et al.* Stacking-fault strengthening of biomedical Co–Cr–Mo alloy via multipass thermomechanical processing. Scientific Reports 2017; 7(1): 1–13.
58. Lu K, Lu L, Suresh S. Strengthening materials by engineering coherent internal boundaries at the nanoscale. Science 2009; 324(5925): 349–352.
59. Jiang B, Qi X, Yang S, *et al.* Effect of stacking-fault probability on martensitic transformation and shape memory effect in Fe-Mn-Si based alloys. Acta Materialia 1998; 46(2): 501–510.
60. Mahato B, Shee SK, Sahu T, *et al.* An effective stac- king fault energy viewpoint on the formation of extended defects and their contribution to strain hardening in a Fe–Mn–Si–Al twinning-induced plasticity steel. Acta Materialia 2015; 86: 69–79.
61. Valiev RZ, Islamgaliev RK, Alexandrov IV. Bulk nanostructured materials from severe plastic deformation. Progress in Materials Science 2000; 45(2): 103–189.
62. Liao X, Zhao Y, Zhu Y, *et al.* Grain-size effect on the deformation mechanisms of nanostructured copper processed by high-pressure torsion. Journal of Applied Physics 2004; 96(1): 636–640.
63. Azushima A, Kopp R, Korhonen A, *et al.* Severe plastic deformation (SPD) processes for metals. CIRP Annals 2008; 57(2): 716–735.
64. Lugo N, Llorca N, Cabrera JM, *et al.* Micro structures and mechanical properties of pure copper deformed severely by equal-channel angular pressing and high pressure torsion. Materials Scien-

ce & Engineering A 2008; 477(1-2): 366–371.
65. Liao X, Zhou F, Lavernia EJ, *et al.* Deformation mechanism in nanocrystalline Al: Partial dislocation slip. Applied Physics Letters 2003; 83(4): 632–634.
66. Lee ML, Simmonds PJ. Tensile strained III-V self-assembled nanostructures on a (110) surface. Nano-epitaxy: Homo- and Heterogeneous Synthesis, Characterization, and Device Integration of Nano-materials 2010; 7768: 5.

Characterization and Application of Nanomaterials (2020) Volume 3 Issue 1
doi:10.24294/can.v3i1.742

ORIGINAL RESEARCH ARTICLE

Hybrid magnetic materials based on polyethylene containing Co and Ni nanoparticles

Alexander Yu. Vasil'kov, Alexander V. Budnikov, Alexander V. Naumkin*

Nesmeyanov Institute of Organoelement Compounds, Russian Academy of Sciences, 28 Vavilov st., Moscow 119991, Russia. E-mail: naumkin@ineos.ac.ru

ABSTRACT

New hybrid magnetic materials based on HDPE filled with Co and Ni nanoparticles have been prepared via the metal vapor synthesis. Properties of the metal-polymer composites have been elucidated as a function of MVS parameters and metal nature. The Faraday method has been applied to characterize the magnetic properties of the systems. The microstructure of the samples has been studied with a number of X-ray and synchrotron techniques, including XRD, EXAFS and SAXS. Core-level and valence band spectra were measured by XPS. The peak at binding energy of 282.8 eV characteristic of C-Ni bond was recorded in the C 1s spectrum. It was shown that properties of nanocomposite materials with similar compositions are determined both by the synthesis conditions and post-synthesis factors.

Keywords: Hybrid Material; Magnetic Properties; HDPE; Cobalt; Nickel; Nanoparticles; Metal Vapor Synthesis; XPS

ARTICLE INFO

Article history:
Received 13 April 2020
Received in revised form 8 May 2020
Accepted 10 May 2020
Available online 27 May 2020

1. Introduction

The metal vapor synthesis (MVS) is an efficient means of purposeful synthesis of nanosized mono-bimetallic particles as well as their derived composites. Modification of polymers with metal nanoparticles give rise to a complex of new functional properties, *e.g.*, magnetic, catalytic, antibacterial ones, *etc*[1-4].

In the vast majority of cases, processing of metal-filled polymers into target products imply an intense external action of temperature, high pressure, reactive chemicals, *etc*.

The present paper reports on the synthesis and characterization of composites derived from high-density polyethylene (HDPE) (M = $2 \cdot 10^5$) filled with Co and Ni nanoparticles prepared by the MVS method. The presence of ferromagnetic species enables the use of the magneto-static measurements (*i.e.*, the Faraday method) to characterize their bulk magnetic propertis[5]. The structure of the materials is studied using X-ray and synchrotron techniques, *viz*., X-ray diffraction (XRD), Extended X-ray Absorption Fine Structure (EXAFS) and Small Angle X-ray Scattering (SAXS)[6].

2. Experimental

A typical MVS reactor[1-4] has an evacuated volume of 5L. Nickel or cobalt samples (0.3-0.5 g) are evaporated into vacuum of 10^{-2} Pa with a W evaporator. Metal vapor is allowed to condense at the reactor walls cooled down to 77 K simultaneously with toluene (100-120 ml). Prior to the synthesis, toluene has been distilled over sodium under Ar

and further degassed in vacuo by several consecutive freeze-pump-thaw cycles. After the synthesis, the reactor walls are allowed to heat up and the metal-toluene ice is transferred right upon melting into jelly-like HDPE-toluene mixture. Metal-polymer composites have been prepared by two methods **A** and **B**, the respective conditions are detailed in **Table 1** and Scheme (See **Figure 1**). Magnetization measurements have been performed in Ar or in vacuum, using the Faraday method[5] over a temperature range of 77-573 K at a magnetic field of 500-3200 Oe.

Table 1. Preparation conditions for metal-HDPE composites
a - stirring of suspensions with a magnetic stirrer (MS) under ultrasonication (US); b - in all cases the organic reagent is toluene

Sample	Metal	Amount of metal, wt %	Means of influence[a] (temperature, K)	Method[b]
1, 2	Co	3.5; 4.6	MS (363)	A
3, 4	Ni	1.4; 4.3	MS (363)	A
5	Co	2.5	US (185)	B
6, 7	Co	12.7; 20.0	MS (363)	A

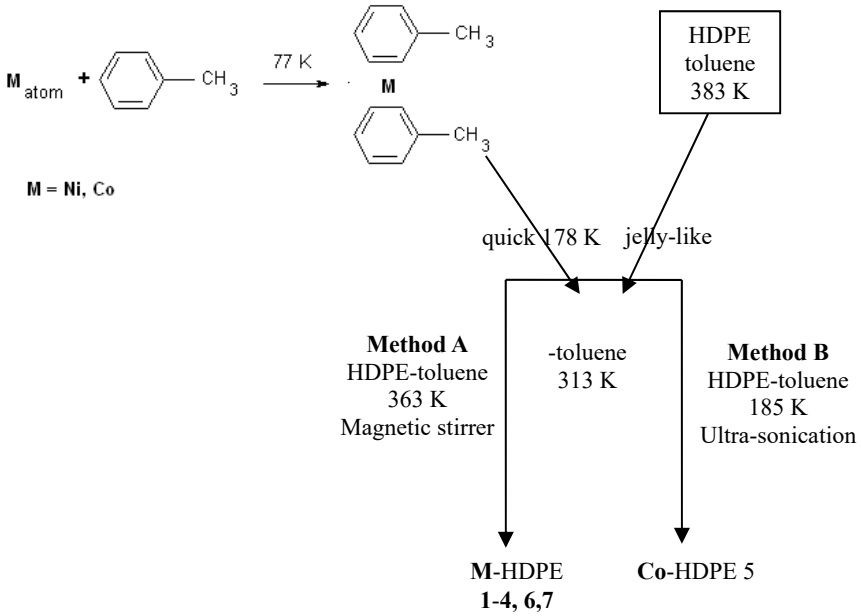

Figure 1. Scheme.

EXAFS and SAXS measurements have been performed at the Structural Materials Science station of the Kurchatov Centre for Synchrotron Radiation and technologies. For both techniques, the transmission geometry was utilized. X-ray beam was monocropmatized with a Si(111) channel-cut monochromator. X- ray diffraction patterns were measured on a laboratory DRON-3 (Russia) diffractometer equipped with a graphite secondary-beam monochromator and NaI(Tl) scintillator counter, using Cu $K_{\alpha 1,2}$ radiation. TGA was carried out with a "Derivatograph-Q1500D" (MOM, Hungary) at a heating rate of 5 °C/min in air on sample loads of about 60 mg.

X-ray photoelectron spectroscopy was performed with an XSAM-800 spectrometer (Kratos, UK), and Al Kα radiation was recorded in a fixed transmission mode of the analyzer. The spectra were measured with step size of 0.1 eV at 20 °C and a pressure in the analytical chamber of $5 \cdot 10^{-8}$ Pa. The photoelectron spectra were approximated by Gauss function or the sum of Gauss functions, and the background caused by secondary electrons and photoelectrons that lost energy, was approximated by the straight line. The energy scale of spectrometer was calibrated according to the standard procedure, taking into account the following binding energies: 932.7, 368.3 and 84.0 eV for $Cu2p_{3/2}$, $Ag3d_{5/2}$, and $Au4f_{7/2}$, respectively. Atomic sensitivity factor (ASF) in spectrometer software was used for quantification. Sample charging was corrected by referencing to the C-C/C-H peak in the C 1s spectrum (284.8 eV).

3. Results and discussion

In the initial phase of MVS, the interaction of metal vapor with toluene in both methods provides a thermally unstable Co or Ni complex (see **Figure 1**). Resultant toluene solutions of these complexes after the synthesis were transferred into the jelly-like HDPE-toluene mixtures pre-pared by boiling polyethylene in toluene under argon followed by cooling of the mixtures down to 363 and 185 K.

The synthetic route **A** initiates rapid thermal decomposition of the complexes in the bulk of the polymer at a temperature by far exceeding the decomposition point. Metal nanoparticles fill curves and defects that exist in the polymer and are held in place by space or other factors.

Effects of temperature on the properties of the composites were controlled by magnetostatic measurements. Thermomagnetic curves for Ni-HDPE systems (see **Figure 2**) demonstrate reversible behavior over 80-370 K. An increase in temperature up to 420-430 K induces an irreversible drop in magnetization, which is probably due to the interaction of Ni particles with polymer to yield a weaker magnetic phase. Meanwhile, thermomagnetic curves of materials produced by annealing also demonstrate reversible behavior over 300-420 K.

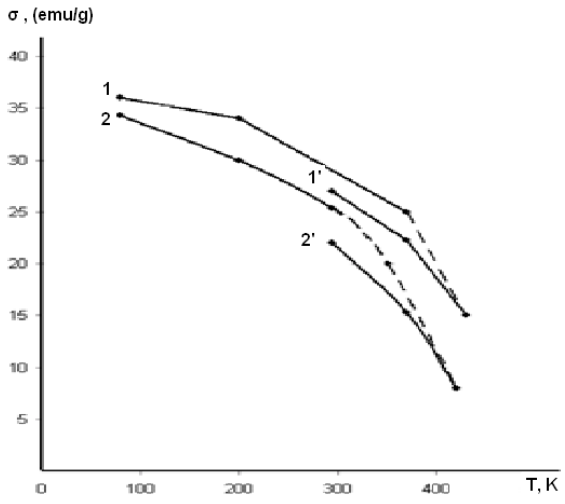

Figure 2. Thermomagnetic curves for Ni-HDPE composites**.**
1 - initial sample 1.4% Ni-HDPE; 2 - initial sample 4.3% Ni-HDPE**.**
1′ and 2′ - after annealing at 430 K and 420 K, respectively.

Co-HDPE samples manifest substantially different magnetic properties. **Figure 3** shows thermomagnetic curves of some representative Co-contaning materials. A composite of 3.5% Co-HDPE exhibits a reversible thermomagnetic curve up to 370K, and demonstrates a decrease in magnetization be a factor of 1.5 upon cooling to 80K.

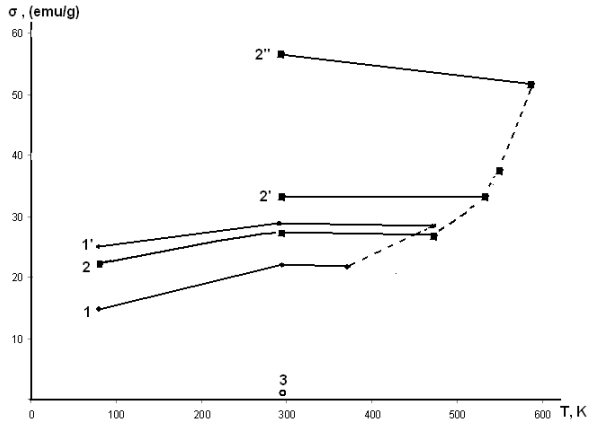

Figure 3. Thermomagnetic curves for selected Co-HDPE composites; 1- initial sample 3.5% Co-HDPE**.**
1′ - after annealing at 470 K; 2 - initial sample 4.6% Co-HDPE; 2′ and 2″- after annealing at 530 K and 585 K, respectively.
3 - sample 2.5% Co-polyethylene maintained at a cryogenic temperature.

An increase in temperature up to 470K results in an irreversible increase in magnetization. This change gives rise to a new thermomagnetic behavior reversible over 80-470K. This is a distinctive signature of the agglomeration of Co particles due to softening of the matrix related to the transition of HDPE into the viscous fluidic state. Further heating gives rise to progressive increase in magnetization of the composite.

Variations of cry-synthesis conditions strongly affect properties of the resultant products. A sample of 2.5% Co-HDPE maintained at cryogenic temperatures (method **B**) is characterized by weak magnetic properties. Its magnetization at room temperature is lower than that of samples with a similar metal content synthesized via the route **A** by a factor of 30-40 (see **Figure 3**). Furthermore, it is characterized by a very weak ferromagnetic resonance signal.

The MVS synthesis of non-ferromagnetic Ni powders upon interaction of metal particles with alkanes has been described earlier. At the same time, cobalt blacks demonstrate totally different behavior[7]. Probably, the application of a lower temperature in the case of the toluene-HDPE

system coupled with ultra-sonication effectively encapsulate very small Co nanoparticles within the polymer shell.

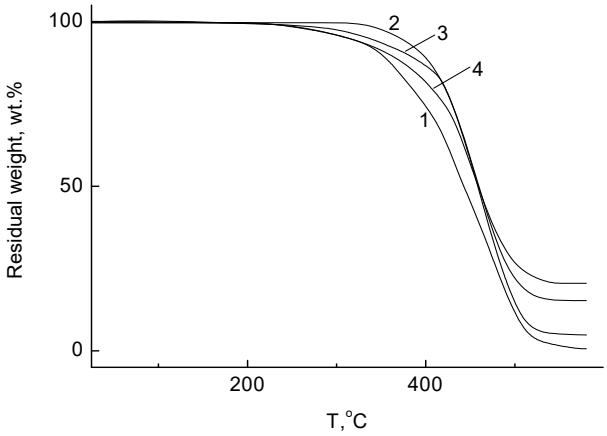

Figure 4. TGA Curves for HDPE Initial (1) and with 3.5 (2), 12.7 (3), and 20 wt.% of Co at a Heating Rate of 5 °C/min in air**.**

Thermal characteristics of the nanocomposites have been studied by TGA (**Figure 4**). It has been established that the introduction of Co into HDPE inhibits its thermos-oxidative decomposition. The decomposition point related to a 5% mass loss ($T_d^{5\%}$) in the case of metal-filled composites shifts to a higher temperature as compared to pristine HDPE. The thermos-oxidative resistivity of the nanocomposites appears roughly inversely proportional to the metal content. Indeed the composite containing 3.5 wt.% of Co is characterized by $T_d^{5\%}$ as high as 365 °C, whereas Co 12.7 wt% sample demonstrates $T_d^{5\%}$ of 329 °C, and the 20.0 wt.% sample reveals $T_d^{5\%}$ of 303 °C exactly as in pristine HDPE. Residual weight well correlates with the amount of metal Co introduced into HDPE.

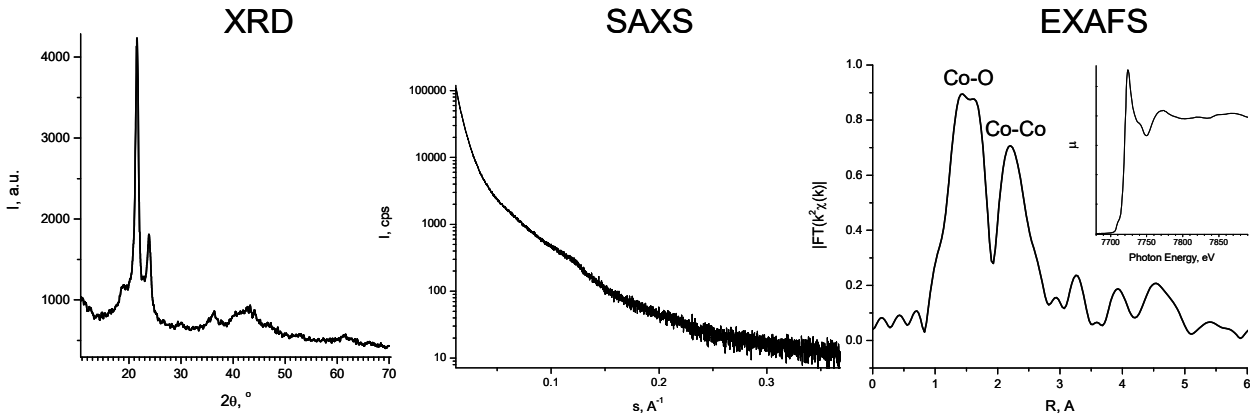

Figure 5. Results of structural characterization of a representative Co-HDPE composite**.**

Some results of structural characterization of the composites are represented in **Figure 5**. Co K-edge EXAFS and XANES data indicate that Co atoms are characterized by mixed oxide-metallic environment which probably means that cobalt nanoparticles have a core-shell structure with a metallic core stabilized inside an oxide or oxide-carbide outer shell. The size of the particles estimated from XRD and SAXS is 3-5 nm.

The thermomagnetic curves of Ni 4.3 wt.% - HDPE composite (**Figure 2, sample 2**) showed a significant decrease in magnetization after heating. This may be due to the appearance of a new non-magnetic phase. To determine the chemical state of the metal in this nanocomposite, a model sample of HDPE powder modified with bis (toluene) nickel as described elsewhere[1,8,9] was prepared.

After the treatment, the toluene was distilled off in a vacuum, and the resulting Ni-HDPE system was studied by XPS. XPS quantification based on ASF gives composition $C_{88.5}O_{9.1}$- $Ni_{2.4}$.

Figure 6 shows the Ni 2p and O 1s photoelectron spectra of Ni-HDPE composite. The Ni 2p spectrum consists of spin-orbit doublet and two satellites. The binding energies of the main Ni $2p_{3/2}$ and $Ni2p_{1/2}$ peaks are 856.7 and 874.4 eV, and the corresponding satellites are at 862.3 and 830.8 eV. The O 1s spectrum exhibits a broad peak at 531.4 eV which can be fitted with three Gaussian peaks at 531.0, 532.3 and 533.3 eV with Gaussian width of 2.14 eV and relative intensities of 46:49:5. The peak at 531.0 eV represents the bound hydroxide groups OH, while those at 532.5 and 533.3 eV represent O-C bonds and water. Taking into account characteristics of photoe-

lectron spectra compiled in **Table 2**[10-22], such as binding energies (E_b) of main and satellite peaks, satellite shifts (ΔE_1 = E_b(Ni $2p_{3/2}$ sat) - E_b(Ni $2p_{3/2}$) and ΔE_2 = E_b(Ni $2p_{1/2}$ sat) - E_b(Ni $2p_{1/2}$), spin-orbit splitting (ΔE_3 = E_b(Ni $2p_{1/2}$) – E_b(Ni $2p_{3/2}$), an energy interval between Ni $2p_{3/2}$ and O 1s peaks (ΔE_4 = E_b(Ni $2p_{3/2}$) – E_b(O 1s)), we have assigned the Ni $2p_{3/2}$ spectrum to $Ni(OH)_2$ phase.

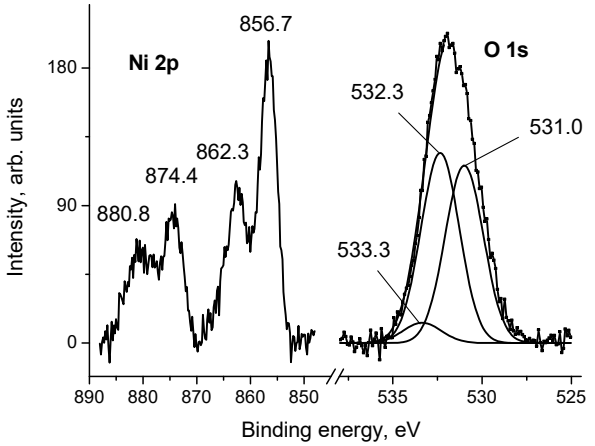

Figure 6. The Ni 2p and O 1s photoelectron spectra of Ni-HDPE composite**.**

In case of NiO, according to NIST XPS Database, the Ni $2p_{3/2}$ peak position is within value range of 853.4 – 856.5 eV[23] while that of O 1s is at 528.9-530.7 eV. It should be noted that reliable assignment we have compiled only data with satellite shifts. To discriminate between NiO and $Ni(OH)_2$, we compared Ni 2p line shape as well[24-26]. The Ni 2p binding energies of Ni-HDPE composite compared with those in **Table 1** show positive shift relative to the reference data. For the Ni/SiO_2 nanocomposite prepared by similar way, the chemical shift was less by 0.8 eV[8,9].

This indicates a different character of the interaction of nickel nanoparticles with polyethylene and SiO_2. A possible reason for this difference may be the presence of a large amount of oxygen in SiO_2 in comparison with polyethylene and the manifestation of differential charging. Another reason may be a large concentration of hydrogen in the polyethylene, which promotes the predominant formation of $Ni(OH)_2$. The last hypothesis that can be confirmed by the appearance of a signal at 282.8 eV in the C 1s spectrum can be assigned to Ni-C bond.

The C 1s spectrum was fitted with four states at 282.8, 285.0, 286.5 and 288.5 eV with Gaussian widths of 1.54, 1.81, 1.81 and 1.98 eV and relative intensities of 6:85:8:1, respectively (See **Figure 7**). The peak at 285.0 eV represents the C-C/ C-H bonds of polyethylene, while those at 265.5 and 288.5 eV represent C-O and C(O)O groups of oxidized carbon atoms. Therefore, the C 1s spectrum indicates strong electronic interactions between Ni and carbon atoms.

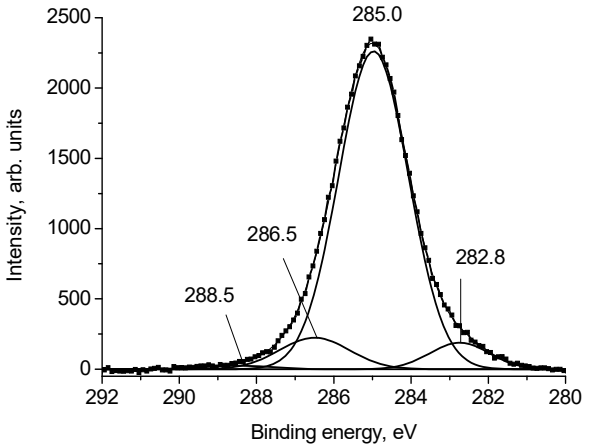

Figure 7. The C 1s photoelectron spectrum of Ni-HDPE composite**.**

This $Ni(OH)_2$-C interface is also an important factor to reflect the magnetic properties of Ni-PE composites. It should be noted that because the difference in kinetic energy determines the inelastic mean free path of electrons, C 1s photoelectrons have higher surface sensitivity than Ni 2p photoelectrons. The XPS analysis of the data for the Ni-HDPE composite showed that along with the metal oxidation process, the destruction of the polymer matrix and the formation of the C-Ni state occur. The probability of these processes increases significantly with increasing temperature. This can lead to the formation of a metal-carbon non-magnetic phase, the effect of which, apparently, appears in the study of magnetic properties. Co-HDPE nanocomposite was analysed by the XPS method. In the survey spectrum of the sample, no characteristic peaks of Co were observed. This indicates the presence of metal nanoparticles at a depth exceeding the information depth of photoelectrons Co 2p.

Table 2. XPS characteristics of Ni compounds: binding energies of different peaks (E_b), satellite splitting ($\Delta E_{1,2}$), spin–orbit splitting (ΔE_3) and $\Delta E_4 = E_b(\text{Ni } 2p_{3/2}) - E_b(\text{O } 1s)$; all the energies are in eV

Sample	Ni $2p_{3/2}$	Ni $2p_{3/2}$ sat	ΔE_1	Ni $2p_{1/2}$	Ni $2p_{1/2}$ sat	ΔE_2	ΔE_3	O 1s	ΔE_4	Assignment for O 1s	Ref.
NiO	853.6 855.4	860.7	7.1					529.2			10
NiO	853.9 855.5	860.6	6.7					529.4			11
NiO	854.1 856.0	861.6	7.5					529.6			12
NiO	854.1 856.0	861.2	7.1					529.9			13
NiO	854.4 856.2	860.9	6.5					530.0			14
NiO	854.5 856.6	861.6 864.2	7.1 7.6	872.0 873.9	879.2 881.9	7.2 8.0	17.5	529.6 531.6	325.0	NiO O-C	15
NiO	855.22 857.13	861.42	6.2								16
α-$Ni(OH)_2$	855.5	861.2	5.7	873.1	879.8	6.7	17.6	531.0 532.4	324.5	$Ni(OH)_2$ H_2O, O-C	17
$Ni_2O_3 \cdot 6H_2O$	855.5	861.3	5.8	873.1	879.7	6.6	17.6	529.3 530.8	326.2	Ni_2O_3 $Ni(OH)_2$, O-C	18
γ-NiOOH	855.7	861.5	5.8	873.2	879.8	6.6	17.5	531.0 532.8	324.7	NiOOH H_2O, O-C	19
$Ni(OH)_2$	855.9	861.7	5.8	873.6	880.0	6.4	17.7	529.4 532.2	326.5	$Ni(OH)_2$, H_2O, O-C	20
Ni/SiO_2	855.9	861.5	5.6					531.5	324.4	Ni-O	1,8, 9
β-$Ni(OH)_2$	856.2	861.8	5.6	873.8	880.1	6.3	17.6	531.0	325.2	$Ni(OH)_2$	21
$Ni(OH)_2$	856.5	862.4	5.9	874.1	880.6	6.5					22
$Ni(OH)_2$	856.7	862.3	5.6	874.4	880.8	6.4	17.7	531.0 534.5	325.7	$Ni(OH)_2$ O-C	this work

Note: $\Delta E_1 = E_b(\text{Ni } 2p_{3/2} \text{ sat}) - E_b(\text{Ni } 2p_{3/2})$, $\Delta E_2 = E_b(\text{Ni } 2p_{1/2} \text{ sat}) - E_b(\text{Ni } 2p_{1/2})$, $\Delta E_3 = E_b(\text{Ni } 2p_{1/2}) - E_b(\text{Ni } 2p_{3/2})$, $\Delta E_4 = E_b(\text{Ni } 2p_{3/2}) - E_b(\text{O } 1s)$.

The inelastic mean free path length (λ) of Co 2p photoelectrons in pure Co is ~ 12 Å[27], while that in polyethylene is ~ 27 Å[28], and the corresponding information depth 3λ is ~ 81 Å. Because λ of the valence band and the C 1s photoelectrons is more than that of Co 2p photoelectrons, they are analyzed as well.

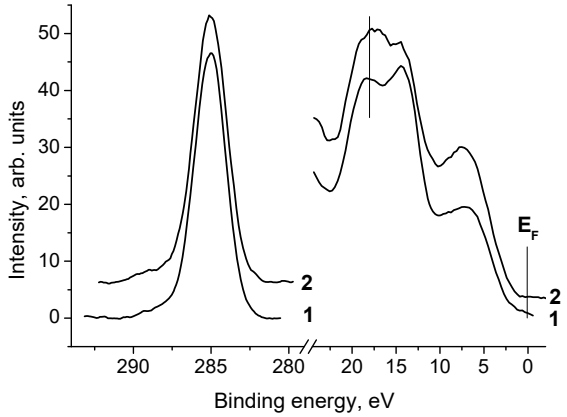

Figure 8. C 1s and valence band spectra of HDPE (1) and Co-HDPE nanocomposite (2)

The introduction of Co into polyethylene leads to an insignificant broadening of the C 1s peak, while significant changes in the valence band spectrum are observed (**Figure 8**). These changes reflect the change in the density of states near the Fermi level. **Figure 8** shows the C 1s and valence band spectra of HDPE and HDPE-Co nano-composite. The C 1s spectrum of HDPE can be fitted with three Gaussian peaks at 285.0, 285.6 and 288.4 eV with width of 1.98 eV and relative intensities of 93:4:3. The peaks are as-signed to C-C/C-H, C-O and C(O)O groups, respectively. The C 1s spectrum of HDPE-Co nanocomposite can be fitted with three Gaussian peaks at 285.0, 285.6 and 288.7 eV with width of 2.04 eV and relative intensities of 91:5:4.

Figure 9 shows the O 1s spectrum fitted with three peaks at 529.4, 532.4 and 534.5 eV with width of 2.14 eV and relative intensities of 4:87:9. The peak at 532.4 eV is assigned to oxidized carbon atoms of HDPE, while that at 534.5 eV is assigned to chemisorbed water. The peak at 529.4 eV could be assigned to physisorbed water and/or O-Co bonds[23,29,]. However, the latter assignment

is less probable because of small difference in inelastic mean free paths of the Co 2p and O 1s electrons and great difference in ASF[30].

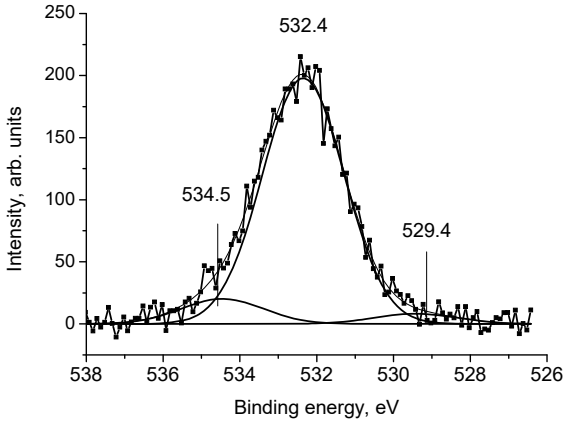

Figure 9. The O 1s spectrum of Co-HDPE nanocomposite**.**

4. Conclusion

The results presented above demonstrate that properties of nanocomposite materials with similar compositions are determined both by the synthesis conditions and post-synthesis factors, which has to be necessarily taken into account in their further processing.

An XPS analysis of the Ni-HDPE system showed formation of Ni-C bonds. When heated, this process accelerates. It can lead to the formation of a phase with lower magnetic characteristics. The Co-HDPE system behaves differently. Its heating is accompanied by an increase in the magnetization, which can be caused by the aggregation of metallic particles.

Acknowledgments

This work was supported by the Presidium of the Russian Academy of Sciences (Program "Nanostructures: physics, chemistry, biology, technology fundamentals"). The authors thank Dr. Sc. Yan V. Zubavichus for measurement and analysis of the XRD, EXAFS and SAXS data. Elemental analysis was performed using the equipment at the INEOS RAS Molecular Structure Research Centre.

References

1. Vasil'kov AY, Migulin DA, Naumkin AV, *et al.* Preparation of novel hybrid materials based on core-shell polyorganosilsesquioxanes modified with iron nanoparticles. Mendeleev Communications 2016; 26(3): 187–190.
2. Rubina MS, Kamitov EE, Zubavichus YV, *et al.* Collagen-chitosan scaffold modified with Au and Ag nanoparticles: Synthesis and structure. Applied Surface Science 2016; 366: 365–371.
3. Tsodikov MV, Ellert OG, Nikolaev SA, *et al.* The role of nanosized nickel particles in microwave-assisted dry reforming of lignin. Chemical Engineering Journal 2017; 309: 628–637.
4. Rubina MS, Vasil'kov AY, Naumkin AV, *et al.* Synthesis and characterization of chitosan–copper nanocomposites and their fungicidal activity against two sclerotia-forming plant pathogenic fungi. Journal of Nanostructure in Chemistry 2017; 7: 249–258.
5. Selwood PW. Chemisorption and magnetization. New York: Academic Press; 1975. p. 164.
6. Chernyshov AA, Veligzhanin AA, Zubavichus YV. Structural materials science end-station at the Kurchatov Synchrotron Radiation Source: Recent instrumentation upgrades and experimental results. Nuclear Instruments & Methods in Physics Research 2009; 603(1-2): 95–98.
7. Davis SC, Severson SJ, Klabunde KJ. Clustering of metal atoms in organic media. 8. Low-temperature cleavage of alkanes by small nickel particles resulting in stable nickel-organic composites with unusual magnetic and chemical properties. Journal of American Chemical Society 1981; 103(11): 3024–3029.
8. Naumkin AV, Vasil'kov AY, Volkov IO, *et al.* X-ray photoelectron spectra and structure of composites prepared via deposition of Au, Ni, and Au + Ni nanoparticles on SiO_2 from colloidal solutions in triethylamine. Inorganic Materials 2007; 43(4): 381–385.
9. Vasil'kov AY, Nikolaev SA, Smirnov VV, *et al.* An XPS study of the synergetic effect of gold and nickel supported on SiO_2 in the catalytic isomerization of allylbenzene. Mendeleev Communications 2007; 17(5): 268–270.
10. Lian K, Thorpe SJ, Kirk DW. Electrochemical and surface characterization of electrocatalytically active amorphous Ni-Co alloys. Electrochimica Acta 1992; 37(11): 2029–2041.
11. Venezia AM, Bertoncello R, Deganello G. X-ray photoelectron spectroscopy investigation of pumice-supported nickel catalysts. Surface & Interface Analysis 1995; 23(4): 239–247.
12. Workie B, Kounaves SP, Aksu ML, *et al.* Electrodeposition of metal alloy and mixed oxide films using a single-precursor tetranuclear copper-nickel complex. Journal of The Electrochemical Society 1995; 142(10): 3357–3365.
13. Bianchi CL, Cattania MG, Villa P. XPS characterization of Ni and Mo oxides before and after "in situ" treatments. Applied Surface Science 1993; 70-71(93): 211–216.
14. McIntyre NS, Chan TC, Chen C. Characterization of oxide structures formed on nickel-chromium

alloy during low pressure oxidation at 500-600°C. Oxidation of Metals 1990; 33(5-6): 457–479.
15. Mansour AN. Characterization of NiO by XPS. Surface Science Spectra 1994; 3(3): 239–246.
16. Lian KK, Kirk DW, Thorpe SJ. Investigation of a "Two-State" Tafel Phenomenon for the oxygen evolution reaction on an amorphous NiCo alloy. Journal of The Electrochemical Society 1995; 142(11): 3704–3712.
17. Mansour AN, Melendres CA. Characterization of α-$Ni(OH)_2$ by XPS. Surface Science Spectra 1994; 3(3): 255–262.
18. Mansour AN, Melendres CA. Characterization of $Ni_2O_3 \cdot 6H_2O$ by XPS. Surface Science Spectra 1994; 3(3): 263–270.
19. Mansour AN, Melendres CA. Characterization of electrochemically prepared γ-NiOOH by XPS. Surface Science Spectra 1994; 3(3): 271–278.
20. Mansour AN, Melendres CA. Characterization of slightly hydrated $Ni(OH)_2$ by XPS. Surface Science Spectra 1994; 3(3): 247–254.
21. Mansour AN. Characterization of β-$Ni(OH)_2$ by XPS. Surface Science Spectra 1994; 3(3): 239–246.
22. Chen X, Chen X, Zhang F, *et al.* One-pot hydrothermal synthesis of reduced graphene oxide/carbon nanotube/α-$Ni(OH)_2$ composites for high performance electrochemical supercapacitor. Journal of Power Sources 2013; 243: 555–561.
23. Naumkin AV, Kraut-Vass A, Gaarenstroom SW, *et al.* NIST X-ray photoelectron spectroscopy database [Internet]. Version 4.1. Gaithersburg: National Institute of Standards and Technology; [created 2000 June 6; updated 2012 Spe 15]. Available from: http://srdata.nist.gov/xps/.
24. Payne BP, Biesinger MC, McIntyre NS. Use of oxygen/nickel ratios in the XPS characterisation of oxide phases on nickel metal and nickel alloy surfaces. Journal of Electron Spectroscopy And Related Phenomena 2012; 185(5-7): 159–166.
25. Payne BP, Biesinger MC, McIntyre NS. The study of polycrystalline nickel metal oxidation by water vapour. Journal of Electron Spectroscopy & Related Phenomena 2009; 175(1-3): 55–65.
26. Biesinger MC, Lau LWM, Gerson AR, *et al.* The role of the Auger parameter in XPS studies of nickel metal, halides and oxides. Physical Chemistry Chemical Physics 2012; 14(7): 2434–2442.
27. Tanuma S, Powell CJ, Penn DR. Calculations of electron inelastic mean free paths. IX. Data for 41 elemental solids over the 50 eV to 30 keV range. Surface and Interface Analysis 2011; 43(3): 689–713.
28. Powell CJ, Jablonski A. NIST electron inelastic-mean-free-path database 71 [Internet]. Version 1.1. Gaithersburg: National Institute of Standards and Technology; [created 2000 June 15; updated 2017 Feb 17]. Available from: https://www.nist.gov/publications/nist-electron-inelastic-mean-free-path-database-71-version-11
29. Henderson MA. The interaction of water with solid surfaces: fundamental aspects revisited. Surface Science Reports 2002; 46(1): 1–308.
30. Moulder JF, Stickle WF, Sobol PE, *et al.* Handbook of X-ray photoelectron spectroscopy: a reference book of standard spectra for identification and interpretation of XPS data. In: Chastain J (editor). Eden Prairie, Minnesota: Physical Electronics Division, Perkin-Elmer Corporation; 1992. p. 261.

Characterization and Application of Nanomaterials (2020) Volume 3 Issue 1
doi:10.24294/can.v3i1.554

REVIEW ARTICLE

Characterization and applications of diamond-like nanocomposites: A brief review

Kalyan Adhikary[1], Sayan Das[1,2], Debasish De[1], Anup Mondal[2,3], Utpal Gangopadhyay[1], Sukhendu Jana[1,3*]

[1]*Center for Advanced Research in Renewable Energy and Sensor Technology, Meghnad Saha Institute of Technology, Kolkata 700150, India. Email: sukhendu123@gmail.com*

[2]*Department of Chemistry, Indian Institute of Engineering Science and Technology, Shibpur 713212, India.*

[3]*Centre of Excellence for Green Energy and Sensor System, Indian Institute of Engineering Science and Technology, Shibpur 713212, India.*

ABSTRACT

Diamond-like Nanocomposites (DLN) is a newly member in amorphous carbon (a:C) family. It consists of two or more interpenetrated atomic scale network structures. The amorphous silicon oxide (a:SiO) is incorporated within diamond-like carbon (DLC) matrix i.e. a:CH and both the network is interpenetrated by Si-C bond. Hence, the internal stress of deposited DLN film decreases remarkably compare to DLC. The diamond-like properties have come due to deform tetrahedral carbon with sp^3 configuration and high ratio of sp^3 to sp^2 bond. The DLN has excellent mechanical, electrical, optical and tribological properties. Those properties of DLN could be varied over a wide range by changing deposition parameters, precursor and even post deposition treatment also. The range of properties are: Resistivity 10^{-4} to 10^{14} Ωcm, hardness 10–22 GPa, coefficient of friction 0.03-0.2, wear factor 0.2-0.4 $10^{-7}mm^3/Nm$, transmission Vis-far IR, modulus of elasticity 150-200 GPa, residual stress 200-300 Mpa, dielectric constant 3-9 and maximum operating temperature 600°C in oxygen environment and 1200°C in O_2 free air. Generally, the PECVD method is used to synthesize the DLN film. The most common procedures used for investigation of structure and composition of DLN films are Raman spectroscopy, Fourier transformed infrared spectroscopy (FTIR), HRTEM, FESEM and X-ray photo electron spectroscopy (XPS). Interest in the coating technology has been expressed by nearly every industrial segment including automotive, aerospace, chemical processing, marine, energy, personal care, office equipment, electronics, biomedical and tool and die or in a single line from data to beer in all segment of life. In this review paper, characterization of diamond-like nanocomposites is discussed and subsequently different application areas are also elaborated.

Keywords: Amorphous Carbon; DLC; DLN; PECVD etc.

ARTICLE INFO

Article history:
Received 29 January 2020
Received in revised form 23 February 2020
Accepted 27 February 2020
Available online 11 March 2020

1. Introduction

Carbon is a fascinating element in nature. It has so many allotropes with versatile properties. Diamond, graphite, graphene, carbon nanotube, fullerene, etc. are made by carbon atoms but different structures and bonding hence unique their properties. Diamond is a crystalline allotrope of carbon with unique properties. Diamond has highest hardness and thermal conductivity compared to any bulk material. These properties result from the strong covalent bonding within its atoms and crystal structure. However, diamond cannot be synthesized in room temperature and atmospheric pressure. To synthesize it in lab, same environment to be created as at the depth of 140 to 190 km in the Earth's mantle. To overcome this problem, diamond-like materials are developed which can be synthesized in lab environment and at the

same time exhibits some properties closely resemblance with natural diamond. Diamond-like materials' chemical bonding i.e. mostly sp^3 states complies with natural diamond. Due to this closeness in chemical bonding, diamond-like material shows close resemblance in case of chemical inertness, hardness, thermal stability, thermal conductivity etc. in comparison with natural diamond.

Diamond-like or graphite-like are the umbrella terms which refer to different forms of amorphous carbon that exhibit some of the unique properties of natural diamonds or graphite and that can be synthesized in the lab environment. Diamond-like carbon or DLC is an amorphous hydrogenated carbon which is a blend of sp^2 bonded carbon atoms into sp^3 bonded carbon clusters. In DLC atomic structure, hydrogen can be present with an atomic concentration ranges from 0% to 50%. DLC acronym was first used by Aisenberg and Chabot[1] who for the first time synthesized amorphous carbon films exhibiting some of the unique characteristics of natural diamond. Beauty of the DLC film is that, its properties can be tailored based on the concentration of sp^2 – sp^3 bonded carbon atoms and hydrogen concentration. Due to the room temperature deposition possibility, almost all materials those are compatible with vacuum environment can be coated with DLC films. Unique and tunable properties of DLC are: material hardness, low friction and high wear resistance, chemical inertness, optical transparency (visible light – infrared light), thermal conductivity, electrical resistivity, radiation resistance etc. Most of the present industrial applications of DLC films are protective coating but this application can be extended up to "data to beer storage"[2,3]. However, the major limitation of application of DLC is high internal stress leads to peel off from substrate. Moreover, its thermal stability is also very poor. Sp^3 bonds transform to sp^2 bond at around 300°C. Those difficulties of DLC films could be controlled further by doping them with different chemical elements or compounds like silicon, oxygen, etc. Thus, a new class of amorphous hydrogenated carbon is formed whose chemical bonding complies with crystalline diamond and wisely termed as diamond-like nanocomposite or DLN.

DLN consists of two interpenetrating networks. One is atomic scale diamond-like (carbon network), a-C:H, and another is quartz-like (silicon network), a-Si:O. Carbon network mainly consists of sp^3 hybridization, i.e. diamond-like bonds are chemically stabilized by "H" atoms. In silicon network, Si atoms are chemically stabilized by "O" atoms[4]. Due to the presence of quartz-like oxygenated silicon network (a-Si:O), it is found that DLN has good adhesion property comparing to its predecessor DLC and hence it is suitable to coat almost any type of materials[5]. Due to the interpenetrating network of hydrogenated carbon and oxygenated silicon, the internal stress is reduced and thus DLN composite shows good tribological performance over its predecessor DLC.

DLN coatings have been in existence since early 1990s. V.F. Dorfman first reported and synthesized this unique class of material[4]. Later on Bekaert Advanced Coating Technologies (formerly known as Advanced Refractories Technologies) and Russian and American scientists patented DLN coatings for various protective coatings applications[6-15]. Bekaert Advanced Coating Technologies, Belgium used plasma enhanced chemical vapor deposition (PECVD) method for growing such composite films. Chinese researchers have successfully used ion beam technology for growing DLN films[16]. South Korean researchers have reported thermally activated CVD process for growth of DLN films[17]. DLN coatings also have been used in micro-electromechanical systems (MEMS) applications like LIGA (German acronym for Lithographie, Galvano-formung und Abformung) structures[18]. Moreover, diamond-like carbon/nanosilica composite films have been deposited on silicon substrates, making use of the electrolysis of methanol–dimethylethoxydisilane (DDS) solution at low temperature[19]. DLN coatings also have been used in many applications[20]. DLN was deposited with same type of reactor, used by Bekaert Advanced Coating Technologies, Belgium, by a research group to deposit the thin

film over Co-Cr alloy based knee implant of complex shape[5].

Various researchers have recorded various unique characteristic of DLN thin film since its inception. Yang Won Jae *et al.*[21] reported the relationship of I_D/I_G ratio with structural and mechanical properties of DLN thin film by varying bias voltage from -100V to -400V dc. The thermal stability of diamond-like nano composite coating over a wide temperature range was investigated by Yang *et al*[22]. The performance of DLN film from a tribological perspective was investigated by Venkatraman C *et al*[23]. The performance was satisfactory up to 400°C. Later, Neernick *et al.* in one of their papers stated low-friction, low-wear combined with low internal stress and good adhesion of DLN coating, making it suitable for tribological applications[24]. Again Neernick *et al.* reported low-friction and low-wear behavior of diamond-like nanocomposite coatings even in humid environments. They also reported that DLN film is suitable for industrial applications as hard, self-lubricating coatings on sliding parts in the automotive, chemical, pharmaceutical or biomedical industry[25]. Later, Bozhko A *et al.* showed non-ohmic effects in the electronic transport in tungsten and silicon containing diamond-like films[26]. Sliding wire behavior of DLN was studied by Kester D J *et al*[27]. The dependence of diamond-like atomic scale composite (DLASC) parameter on deposition conditions thermal and radiation treatment was studied and reported by Polyakov VI *et al*[28]. Scharf TW *et al.* investigated the fundamental mechanisms of friction and interfacial shear strength in DLN coatings and the roles of contact stress and environment on their tribological behavior[29]. Roger J. Narayan reported hydroxyapatite which is a bioactive ceramic that mimics the mineral composition of natural bones. Hydroxyapatite diamond-like carbon bilayer film is developed to improve adhesion and mechanical integrity. Thus, hydroxyapatite diamond-like carbon bilayer film serves as a good biomaterial for various orthopedic implant-s[30]. Bursikova Vilma *et al.* recorded laser ablation of nitrogen-doped DLN thin layer, used commercially available MALDI-TOF MS instrumentation and performed identification of ablated species from DLN materials[31]. Mechanical properties of diamond-like nanocomposite thin films on a non-conducting ceramic substrate, here silicon nitride were investigated by A. Pandit *et al.* and hardness and modulus measured by nanoin-dentation and subsequently interfacial toughness of this hard film brittle substrate system were determined by vicker indentation[32]. Venkatraman *et al.* deposited DLN films comprising of C, H, Si, O and metal atoms on metallized silicon substrates via an accelerated plasma approach. They concluded the tailorability of electrical and diamond-like properties of DLN thin film make them suitable for application requiring both wear resistance and electrical tailorability[33]. Scharf *et al.* reported the frictional behavior of amorphous diamond-like nanocomposite coatings in low speed, dry sliding contact using a home-built in-situe Raman tribometer[34]. Hauert R *et al.* investigated on tailored tribological and biological behaviour of DLC[35]. Later, Mallouf R *et al.* reported biocompatibility of DLC and DLN material and showed the application area of DLC and DLN as biosensors[36]. Pollak FH *et al.* showed unique surface and bulk properties of diamond-like atomic scale composite materials deposited on Si (001) substrate through atomic force microscopy investigation[37]. The superiority of DLC coating over different materials used in hip joint prostheses was investigated by Platon F *et al*[38]. Sheeja *et al.* reported the tribological characteristic of surface modified UHMWPE against DLC coated Co-Cr-Mo. Coating both the sliding surfaces of UHMWPE and Co-Cr-Mo with DLC coating reduces the wear rates of the sliding surfaces to a noticable extent[39]. Kobayashi S *et al.* showed the wear properties of DLC coated UHMWPE and PMMA and the result was satisfactory[40]. Later, Logothetidis S compared the haemocompatibility property between amorphous carbon (a-C) and amorphous hydrogenated carbon (a-C:H). Amorphous hydrogenated carbon showed better result as haemocompatible material may be used as biocompatible coatings on biomedical implants[41].

DLN coatings have excellent bulk and surface property as well as thermal stability. This can be used as tribological coatings, chemical protective coatings[23-25,27,34] and abrasion resistant coat-

ings. It has optical transparency over a wide bandwidth which includes visible light and infrared. Due to this reason, DLN coating is used as antireflection coating over the solar cell to enhance the overall efficiency of the system. Due to low residual stress DLN coating has excellent adhesion to variety of substrate materials[30,32]. Researchers at Department of Cardiology, University Hospitals Leuven, Belgium[42] reported the biocompatibility of DLN film resulting in decreased thrombogenicity and decreased neointimal hyperplasia. Awadesh Kr Mallik *et al.* reported that deposition of DLN coating by PECVD method over different substrate used as load bearing orthopedic implant and the result was satisfactory[5].

Since its inception, DLN films are being received huge attention due to its attractive electrical mechanical optical and tribological properties such as reduced stress level, increased thermal stability, high hardness, low friction visible and infrared transparency etc. Dielectric permittivity and refractive index of DLN is lower than the DLC, whereas optical transparency is higher than the DLC films.

In this paper depositions, structure, chemical composition as well as mechanical, optical, electrical, properties of DLN composite films are elaborated and industrial and prospective applications of DLN films are discussed.

2. Deposition method

Two types of thin film deposition methods are generally used, CVD and PVD. On the one hand, in CVD, reactive gases interact with substrate. Generally, it is used to deposit Si and dielectrics. Quality of the deposited film is good and this method has good step coverage. On the other hand PVD is used to deposit metals, and purity of the deposited metal is high. But one disadvantage is that it requires line of sight operation. Various types of CVD are APCVD, LPCVD, PECVD and HDPCVD. Steps in CVD are:

1) Transport reactants via forced convection to reaction region.

2) Transport reactants via diffusion to wafer surface.

3) Adsorb reactants on surface.

4) Surface processes: chemical decomposition, surface migration, site incorporation, etc.

5) Desorption from surface.

6) Transport byproducts through boundary layer.

7) Transport byproducts away from deposition region.

PVD is a versatile deposition method. It can deposit almost any material. Substrate damage is less and very few chemical reactions are required. PVD undergoes some limitations like line of sight operation, shadowing, thickness uniformity and difficult to evaporates materials with low vapour pressure. It has two types, evaporation and sputtering.

3. DLN deposition method

PECVD is mostly used for deposition of DLN film over a substrate surface. PECVD reactor has five rotating substrate holders whose rotating speed can be controlled by a speed controller. Rotation of the substrate holders can be made in two modes, manual and automatic[5]. During substrate attachment on the substrate holder, manual rotation is provided to adjust the position between holder and the operator. Automatic rotation is generally provided during the deposition process. In our PECVD reactor, liquid precursor is fed at the bottom of the vacuum chamber and due to the difference of pressure level between the reactor chamber and the ambience, precursor evaporates into vapour form. An inverted U-shaped tungsten filament is placed over the precursor outlet. Filament is kept at negative potential and it emits electrons which ionize the precursor vapour inside the reactor chamber. Precursor ions are pulled by negatively charged substrate holder where substrates are fixed. Thus precursor ions are finally deposited on the substrate surface and hence substrates are DLN coated. Prior to the coating process, inert gas Ar is introduced into the vacuum chamber to produce the plasma. These argon ions strike the substrate surface and clean the surface by ion etching process.

So, coating process includes the following mandatory steps:

1) Ion etching of the substrate was used to reduce the chance of contamination and better adhesion of coated material over the substrate surface.

2) Vapourization of material to be deposited.

3) Formation of radical of the material to be deposited.

4) Transportation of radicals towards the substrate surface.

5) Deposition/condensation of material onto the substrate surface.

4. Precursors

DLN films can be synthesized using composite materials of silicon and oxygen[43]. These precursors might be gaseous (Silane – (SiH_4) and oxygen (O_2) mix)[44], tetra methyle silane-TMS ($(CH_3)_3SiH$ and oxygen mix)[45] or liquids hexamethyle disiloxane HMDSO ($C_6H_{18}OSi_2$)[46-51], or tetraethoxysilane (TEOS, $(C_2H_5O)_4Si$[52], or tetraethylorthosilicate-TEOS (SiC_8- $H_{20}O_4$)[21,53,54], hexa methyle disilane-HMDS (C_6H_{18}- Si_2)[55] and mixed siloxane and silazane precursors. Liquid precursors are mostly used for their easy handling and various choices[17]. These carbon, silicon, oxygen or nitrogen containing precursors are mixed with hydrocarbon gas (CH_4, C_2H_2 etc) or innert gas Argon (Ar). This mixture is used to coat the substarte under vacuum condition. Silane gas is rarely used as DLN film due to it highly flammable nature and toxicity. So, instead SiH_4, HMDSN, HMDSO are commonly used as precursor liquid now a days due to its less toxicity and flammability.

5. Structure and composition of DLN composite films

Raman spectroscopy, Fourier Transformed Infrared spectroscopy (FTIR) and X-ray photoelectron spectroscopy (XPS) are frequently used techniques to study the structure and chemical composition of synthesized DLN films. Combination of these techniques gives overall information about the structure and composition of DLN thin films. XPS is a surface sensitive quantitative spectroscopic technique that measures the chemical composition, electronic states etc. of the elements presented on the surface of a film. It was found that DLN film consists of carbon, silicon, hydrogen and oxygen, yet it is not possible to determine the amount of hydrogen using XPS technique. Analyzing the position and shape of the peak obtained due to C, Si and O atom, one can draw the quantitative and comprehensive picture of chemical bonding (C-C, Si-C, O-C-O, Si-O) presented in the DLN films[53].

Raman spectroscopy is a fast and non-destructive way to study amorphous carbon as it can reveal the information of clustering of sp^2 phase and orientation of sp^2 phase as well as the hydrogen content[56]. In Raman spectra, all carbons show common features in the (800-2000) cm^{-1} region. G and D peaks lie at ~1560cm^{-1} and ~1360 cm^{-1} respectively in visible excitation and T peak at ~1060 cm^{-1} and visible only for UV excitation[56]. G peak is due to bond stretching of all pairs of sp^2 atoms in both rings and chains. D peak is due to the breathing modes of sp^2 atoms in the rings. T peak is due to the C-C sp^3 vibration[53].

6. Properties

6.1 Mechanical properties

In DLN film, hydrogenated carbon and oxygenated silicon are penetrating to each other in the microstructure of the film. Thus, internal stress substantially is lower in the DLN material[57]. Stress of DLN film deposited using HMDSO precursor vapour by ICP PE-CVD was ~ 15 GPa compared to 11 GPa stress of DLC films diposited using CH_4 gas. Stress can be further decreased by increasing the Si atomic concentartion[52]. Hardness and young modulus are decreased in DLN film in comparison with DLC film[22,45,46,53,54,58,59].

6.2 Coefficient of friction and wear resistance

Study reveals that coefficient of friction of DLN films was lower than DLC films. Coefficient of friction of DLN films does not depend monotonically with chemical composition[24]. Lowest and highest reported coefficient of friction ranges were reported as 0.04-0.08 and 0.1-0.2 respectively. Friction coefficient depends upon substrate bias[53]. Friction of coefficient <0.05 was reported

when substrate bias was in between -100V and -200V and coefficient of friction increase-d >2 times with increase of substrate bias up to -500V.

It is already reported that, wear resistance of DLN with impurity like SiO_x is 15-20 times lower than the wear resistance of DLC film[58]. It has been also reported[5] that wear resistance of DLN film is in the range of 0.2-0.4 compared to wear factor of DLC film 0.5-1. Wear resistance is further decreased with increased concentration of Si and O[24]. In general, DLN film has lower residual stress, lower coefficient of friction in dry as well as humid atmospheres. Deposition parameter must be chosen carefully to fabricate DLN films with desired level of hardness, young's modulus and wear resistance.

6.3 Optical properties

In amorphous hydrogenated carbon (a-C:H), there is a coexistence of sp^2 and sp^3 carbon atoms. So, it has both π and σ electrons. Optical properties of amorphous carbon is determined by π-π* and σ-σ* electronic transitions, along with π-σ* and σ-π* transitions[60]. Optical properties are characterized by optical band gap E_g (Tauc gap), energy E_{04} and Urbach energy E_U. Incorporating Si, O atoms in amorphous carbon (a-C:H) causes change in optical properties like optical band gap and refractive index in the DLN films (a-C:H; a-Si:H). It is reported that increase in optical band gap causes increase in optical transparency[46,62,63].

6.4 Electrical properties

Dielectric constant depends upon different substrates used for deposition of DLN films (Ti, Si, Al, Cr). Such dependence is due to different structure of the films as well as different roughness of the used substrates[64]. Experiment reveals that DLN film has good dielectric properties. DLN films are used as an insulating material in a MIM (Metal-insulator-metal) capacitor and shows good results[65].

Result based on the experiments made by Awadesh Kr Mallik *et al.*[5] are tabulated below:

Table 1. Results of property and range of obtainable values

Property	**Range of obtainable values**
Coefficient of friction	0.03-0.2
Adhesion	107-109 N/m^2 Adhere to a wide range of substrates including metals, plastics and ceramics; no interlayers required
Thermal stability	Stable to 400-600 $^{\circ}C$ in air; capable of 1000-1200 $^{\circ}C$ in absence of oxygen
Physical flexibility	Very flexible; dows not crack when bent
Corrosion and erosion	Resistant to acids, alkalis and particulates due to pore free structure
Electrical resistivity	Undoped:10^{12}-10^{14} Ohm cm; Metal doped: upto 10^{-4} Ohm cm
Hardness	10-22 Gpa
Modulus of elasticity	150-200 Gpa
Residual stress	200-300 Mpa
Transmission	70-80% at 05-20 microns

7. Applications

In DLN, two microstructures (hydrogenated carbon and oxygenated silicon) are interpenetrating each other and thus internal stress is decreased and adhesion property is increased and hence this composite has improved adhesion to almost all kinds of substrates. It has huge application in the field of biomedical implants. This can be used as biomedical sensors as well. DLC coatings can be used as protective wear resistant coating in joint prostheses. Awadesh Kr *et al.* already deposited DLN coatings by PECVD method over various substrates like SS 316 L, glass, Si (100), ceramic (Al_2O_3), ultra-high molecular weight polyethylene (UHMWPE), Co-Cr alloy, Ti_6Al_4V alloy, etc[5]. Most of these materials have been in use as load-bearing orthopedic implants, like hip joint, knee joint, etc[66]. As its coefficient of friction is very less, DLN films can be used as wear resistant coating. As it is anticorrosive, this composite can be used as anti-corrosive coating on wrist watches, brass made show pieces etc. to enhance their longevity. Mechanical properties of DLN material along with the low refractive index and higher transparency compared with other thin film materials, makes DLN an attractive option for choosing DLN as a protective coating[44]. Santra TS *et al.* reported DLN films have their unique number of structural, mechanical and tribological proper-

ties which are quite similar with MEMS material. Due to these unique properties of DLN films, these are suitable for MEMS/NEMS devices manufacturing. The high mechanical properties of DLN films make it applicable for design of high frequency resonator and comb deriver for sensing and actuating applications. DLN film is a biocompatible material. So, we can use DLN films for detection of bio-molecules in biological research and disease diagnosis[67]. Due to its infrared transparency, this can be used as anti-reflective coating on solar cell, glass etc. Sukhendu Jana *et al.*[65] reported diamond-like nanocomposite film behaves as a dielectric medium. DLN thin film based MIM capacitor is applicable for high capacitance and high frequency operation. Thus, DLN thin film MIM capacitor has great potential for use in electrical or electronic circuit. It has already been reported that DLC are used for optical wave guiding sensing systems[68], transistors[69] and high temperature sensing up to 600°C[70]. As DLN is an improved version of DLC, there is a possibility to use DLN for the same purpose. Diamond film grown on p-Si substrates using MWPECVD technique[71-73] may be used as antenna for harsh environment in aviation application. So, in DLN, the highest physical limits of mechanical, electronic and "sensor" properties can be combined and thus smart future material can be constructed. The DLN film has been applied on silicon solar cell as antireflection and passivation coating with significant enhancement of solar cell efficiency[74-75].

8. Conclusion

Diamond-like nanocomposite has become an interesting material due to its tunable unique properties. This material could be deposited on various types of materials by PECVD method at low temperature. The different properties of the film could be varied over wide range by changing deposition parameters, precursor, doping and even post deposition treatment also like annealing. Low residual stress, high hardness, high young modulus and low wear make them a suitable material as wear protecting coating, MEMS, etc. In addition, biocompatibility of the film expands its application to medical area also. C-Si/ a: DLN heterojunction is used to sense different toxic gasses. Recently, this film has been used as an antireflection coating on crystalline silicon solar cell due to its excellent optical property.

Acknowledgement

The authors most sincerely acknowledge the DST, Govt. of India for financial support and Meghnad Saha Institute of Technology for infrastructural support.

References

1. Aisenberg S, Chabot R. Deposition of carbon films with diamond properties. Carbon 1972; 10(3): 356.
2. Robertson J. Diamond-like amorphous carbon. Materials Science and Engineering R Reports 2002; 37(4-6): 129–281.
3. Casiraghi C, Robertson J, Fe Rrari AC. Diamond-like carbon for data and beer storage. Materials Today 2007; 10(1-2): 44–53.
4. Dorfman VF. Diamond-like nanocomposites (DLN). Thin Solid Films 1992; 212(1-2): 267–273.
5. Mallik AK, Dandapat N, Ghosh P, *et al.* Deposition and characterization of diamond-like nanocomposite coatings grown by plasma enhanced chemical vapour deposition over different substrate materials. Bulletin of Materials Science 2013; 36(2): 193–202.
6. Dorfman VF, Boris P (inventors). Dorfman VF (assignee). Method for forming diamond-like nanocomposite or doped-diamond-like nanocomposite films. US patent. 5352493. 1994 Oct 4.
7. Dorfman VF, Boris P (inventors) Dorfman VF (assignee). Diamond-like metallic nanocomposites. US patent 5466431. 1995. Nov 14.
8. Emerson TP, Gu AL (inventors). AlliedSignal Inc. (assignee). Cryogenic turbopump. US patent. 5529464. 1996 June 25.
9. Dorfman VF, Goel A (inventors). Advanced Refractory Technologies, Inc. (assignee). Diamond-like nanocomposite corrosion resistant coatings. US patent. 5728465. 1998 Mar 17.
10. Bosley RW, Miller RF (inventors). Capstone Turbine Corporation (assignee). Hydrostatic augmentation of a compliant foil hydrodynamic fluid film thrust bearing. US patent. 5827040. 1998 Oct 27.
11. Heshmat H (inventors). Mohawk Innovative Technology, Inc. (assignee). High load capacity compliant foil hydrodynamic journal bearing. US patent. 6158893. 2000 Dec 12.
12. Neerinck D, Goel A (inventors). N.V. Bekaert S.A. (assignee). Diamond-like nanocomposite compositions. US patent. 6200675. 2001 Mar 13.
13. Neerinck D, Persoone P (inventors). N.V. Bekaert S.A. (assignee). Coating comprising layers of diamond like carbon and diamond like nanocomposite compositions. US patent. 6228471. 2001 May 8.

14. Jacquet JM, Wietig FG (inventors). Bekaert SN, Jacquet JM, Wietig FG (assignee). Piston ring having hard multi-layer coating. WIPO patent application. WO/2006/125683. 2006 Nov 30.
15. Cooper CV, Tredway WK, Guile RN, *et al* (inventors). United Technologies Corporation (assignee). Cryogenic bearings. US patent. 7296965. 2007 Nov 20.
16. Ding XZ, Zhang FM, Liu XH, *et al.* Ion beam assisted deposition of diamond-like nanocomposite films in an acetylene atmosphere. Thin Solid Films 1999; 346(1-2): 82–85.
17. Yang WJ, Auh KH, Li C, *et al.* Microstructure characteristics of diamond-like nanocomposite (DLN) film by thermally activated chemical vapor deposition. Journal of Materials Science Letters 2000; 19(18): 1649–1651.
18. Prasad SV, Christenson TR, Dugger MT, *et al.* The reality of dynamic interfaces in LIGA microsystems. American Society for Precision Engineering 2003; 28: 43–47.
19. Yan X, Xu T, Chen G, *et al.* Synthesis of diamond-like carbon/nanosilica composite films by an electrochemical metho. Electrochemistry Communications 2004; 6(11): 1159–1162.
20. Santra TS, Bhattacharyya TK, Patel P, *et al.* Structural and tribological properties of diamond-like nanocomposite thin films. Surface & Coatings Technology 2011; 206(2-3): 228–233.
21. Yang WJ, Choa YH, Sekino T, *et al.* Structural characteristics of diamond-like nanocomposite films grown by PECVD. Materials Letters 2003; 57(21): 3305–3310.
22. Yang WJ, Choa YH, Sekino T, *et al.* Thermal stability evaluation of diamond-like nanocomposite coatings. Thin Solid Films 2003; 434(1/2): 49–54.
23. Venkatraman C, Brodbeck C, Lei R. Tribological properties of diamond-like nanocomposite coatings at high temperatures. Surface & Coatings Technology 1999; 115(2-3): 215–221.
24. Neerinck D, Persoone P, Sercu M, *et al.* Diamond-like nanocomposite coatings (a-C:H/a-Si:O) for tribological applications. Diamond & Related Materials 1998; 7(2-5): 468–471.
25. Neerinck D, Persoone P, Sercu M, *et al.* Diamond-like nanocomposite coatings for low-wear and low-friction applications in humid environments. Thin Solid Films 1998; 317(1-2): 402–404.
26. Bozhko A, Chudinov SM, Evangelisti M, *et al.* Non-Ohmic effects in the electronic transport in tungsten- and silicon-containing diamond-like films. Materials Science & Engineering C 1998; 5(3-4): 265–269.
27. Kester DJ, Brodbeck CL, Singer IL, *et al.* Sliding wear behavior of diamond-like nanocomposite coatings. Surface & Coatings Technology 1999; 113(3): 268–273.
28. Polyakov VI, Rukovishnikov AI, Perov PI, *et al.* Optical and electrical properties of metal-diamond-like atomic-scale composite (DLASC) films and DLASC/Si heterostructures. Thin Solid Films 1997; 292(1-2): 91–95.
29. Scharf TW, Ohlhausen JA, Tallant DR, *et al.* Mechanisms of friction in diamondlike nanocomposite coatings. Journal of Applied Physics 2007; 101(6): 143.
30. Narayan RJ. Hydroxyapatite–diamondlike carbon nanocomposite films. Materials Science & Engineering C 2005; 25(3): 398–404.
31. Bursikova V, Rehulkab P, Chmelikb J, *et al.* Laser ablation time-of-flight mass spectrometry (LA-TOF-MS) of "nitrogen doped diamond-like carbon (DLN) nano-layers". Journal of Physics and Chemistry of Solids 2007; 68(5-6): 701–706.
32. Pandit A, Padture NP. Interfacial toughness of diamond-like nanocomposite (DLN) thin films on silicon nitride substrates. Journal of Materials Science Letters 2003; 22(18): 1261–1262.
33. Venkatraman C, Goel A, Lei R, *et al.* Electrical properties of diamond-like nanocomposite coatings. Thin Solid Films 1997; 308-309: 173–177.
34. Jana S, Das S, De D, *et al.* Effect of annealing on structural and optical properties of diamond-like nanocomposite thin films. Applied Physics A 2014; 114(3): 965–972.
35. Hauert R, Muller U. An overview on tailored tribological and biological behavior of diamond-like carbon. Diamond and Related Materials 2003; 12(2): 171–177.
36. Maalouf R, Jaffrezic-Renault N, Vittori O, *et al.* Characterization of different DLC and DLN electrodes for biosensor design. Journal of Advanced Science 2006; 18(1): 31–36.
37. Pollak FH, Dorfman B. Atomic force microscopy study of diamond-like atomic-scale composite films. Thin Solid Films 1997; 292(1-2): 173–178.
38. Platon F, Fournier P, Rouxel S. Tribological behaviour of DLC coatings compared to different materials used in hip joint prostheses. Wear 2001; 250(1-12): 227–236.
39. Sheeja D, Tay BK, Nung LN. Tribological characterization of surface modified UHMWPE against DLC-coated Co-Cr-Mo – ScienceDirect. Surface and Coatings Technology 2005; 190(2-3): 231–237.
40. Kobayashi S, Ozeki K, Hirakuri KK, *et al.* Improvements of wear properties DLC coated UHMWPE and PMMA for biomaterial. Key Engineering Materials 2006; 309-311: 1289–1292.
41. Logothetidis S. Haemocompatibility of carbon based thin films. Diamond and Related Materials 2007; 16(10): 1847–1857.
42. Scheerder ID, Szilard M, Yanming H, *et al.* Evaluation of the biocompatibility of two new diamond-like stent coatings (Dylyn) in a porcine coronary stent model. Journal of Invasive Cardiology 2000; 12(8): 389–394.
43. Meskinis S, Tamuleviciene A. Structure, properties and applications of diamond-like nanocomposite (SiO_x containing DLC) films: A review. Materials Science 2011; 17(4): 358–370.
44. Damasceno JC, Camargo SS. DLC-SiO_x nanocomposite films deposited from CH_4:SiH_4:O_2 gas

mixtures. Surface & Coatings Technology 2006; 200(22-23): 6279–6282.
45. Baek SM, Shirafuji T, Saito N, *et al.* Adhesion property of SiO_x-doped diamond-like carbon films deposited on polycarbonate by inductively coupled plasma chemical vapor deposition. Thin Solid Films 2011; 519(20): 6678–6682.
46. Zajickova L, Bursikova V, Perina V, *et al*. Correlation between SiO_x content and properties of DLC: SiO_x films prepared by PECVD. Surface & Coatings Technology 2003; 174-175: 281–285.
47. Chen LY, Chau-nan Hong F. Effects of SiO_x-incorporation hydrocarbons on the tibological properties of DLC films. Diamond and Related Materials 2001; 10(3-7): 1058–1062.
48. Toth A, Mohai M, Ujvari T, *et al.* Chemical structure of silicon-, oxygen- and nitrogen-containing aC:H films prepared by RF plasma beam CVD. Thin Solid Films 2005; 482(1/2): 188–191.
49. Veres M, Koos M, Toth S, *et al.* Characterisation of a-C:H and oxygen-containing Si:C:H films by Raman spectroscopy and XPS. Diamond and Related Materials 2005; 14(3-7): 1051–1056.
50. Bursikova V, Sladek P, Stahel P, *et al.* Improvement of the efficiency of the silicon solar cells by silicon incorporated diamond-like carbon antireflective coating. Journal of Non-Crystalline Solids 2002; 299(8): 1147–1151.
51. Franta D, Ohlidal I, Bursikova V, *et al*. Optical properties of diamond-like carbon films containing SiO_x. Diamond and Related Materials 2003; 12(9): 1532–1538.
52. Randeniya LK, Bendavid A, Martin PJ, *et al.* Incorporation of Si and SiO_x into diamond-like carbon films: Impact on surface properties and osteoblast adhesion. Acta Biomaterialia 2009; 5(5): 1791–1797.
53. Yang WJ, Sekino T, Shim KB, *et al.* Microstructure and tribological properties of SiO_x/DLC films grown by PECVD. Surface & Coatings Technology 2005; 194(1): 128–135.
54. Randeniya LK, Bendavid A, Martin PJ, *et al*. Molecular structure of SiO_x-incorporated diamond-like carbon films; evidence for phase segregation. Diamond and Related Materials 2009; 18(9): 1167–1173.
55. Santra TS, Liu CH, Bhattacharyya TK, *et al.* Characterization of diamond-like nanocomposite thin films grown by plasma enhanced chemical vapor deposition. Journal of Applied Physics 2010; 107 (12): 541.
56. Ferrari AC, Robertson J. Raman spectroscopy of amorphous, nanostructured, diamond–like carbon, and nanodiamond. Philosophical Transactions of the Royal Society A: Mathematical, Physical and Engineering Sciences 2004; 362(1824): 2477–2512.
57. Chen LY, Hong CN. Effects of SiOx-incorporation hydrocarbons on the tibological properties of DLC films. Diamond and Related Materials 2001; 10(3-7): 1058–1062.
58. Jana S, Das S, Gangopadhyay U, *et al.* A clue to understand environmental influence on friction and wear of diamond-like nanocomposite thin film. Advances in Tribology 2013; 2013(1-4): 1–7.
59. Schiffmann KI, Hieke A. Analysis of microwear experiments on thin DLC coatings: friction, wear and plastic deformation. Wear 2003; 254(5-6): 565–572.
60. Logothetidis S. Optical and electronic properties of amorphous carbon materials. Diamond and Related Materials 2003; 12(2): 141–150.
61. Tamuleviciene A, Meskinis S, Kopustinskas V, *et al.* Optical properties of diamond-like carbon and diamond-like nanocomposite films. Physica Status Solidi 2009; 6(12): 2817–2819.
62. Tamuleviciene A, Meskinis S, Kopustinskas V, *et al.* Diamond-like carbon film as potential antireflective coating for silicon solar cells. Material Sicence (Medziagotyra) 2010; 16(2): 103–107.
63. Tamuleviciene A, Kopustinskas V, Meskinis S, *et al.* Deposition of SiO_x containing DLC films using different transport gas in a closed drift ion beam source program and materials of 3rd international conference “Radiation interaction with materials and its use in technologies”. Kaunas, Lithuania; 2010. p. 169–172.
64. Meskinis S, Slapikas K, Gudaitis R, *et al.* SiO_x-doped DLC films: Charge transport, dielectric properties and structure. Vacuum 2008; 82(6): 617–622.
65. Jana S. Frequency response of Diamond-like nanocomposite thin film based MIM capacitor and equivalent circuit modelling. IOSR Journal of Electrical and Electronics Engineering 2012; 1(2): 46–50.
66. Rahaman MN, Yao A, Bal BS, *et al.* Ceramics for prosthetic hip and knee joint replacement. Journal of the American Ceramic Society 2007; 90(7): 1965–1988.
67. Santra TS, Bhattacharyya TK, Tseng FG, *et al.* Diamond-like nanocomposite (DLN) films for microelectro-mechanical system (MEMS). International Journal of Computer Applications 2011; 6(2): 4.
68. Smietana M, Szmidt J, Dudek M. Application of diamond-Like carbon film in optical waveguide sensing system. Innovative Superhard Materials and Sustainable Coatings for Advanced Manufacturing 2005; 200: 273–279.
69. Wu Y, Lin Y, Bol AA, *et al.* High-frequency, scaled graphene transistors on diamond-like carbon. Nature 2011; 472(7341): 74–78.
70. Santra TS, Bhattacharyya TK, Patel P, *et al.* Diamond, diamond-like carbon (DLC) and diamond-like nanocomposite (DLN) thin films for MEMS applications. Microelectromechanical Systems and Devices. London: InTech; 2012. p. 459–480.
71. Cicala G, Brescia R, Nitti MA, *et al.* Study of polycrystalline diamond deposition by continuous and pulsed discharges. Surface & Coatings Technology 2010; 204(12-13): 1884–1888.

72. Cicala G, Moneger D, Cornacchia D, *et al.* Toward smooth MWPECVD diamond films: Exploring the limits of the hydrogen percentage in $Ar/H_2/CH_4$ gas mixture. Surface & Coatings Technology 2012; 211(3): 152–157.
73. Cicala G, Magaletti BV, Senesi B, *et al.* Smoothness improvement of micrometer- and submicrometer-thick nanocrystalline diamond films produced by MWPECVD. Journal of Nanoparticle Research 2013; 15(4): 1–14.
74. Gangopadhyay U, Jana S, Das S, *et al.* Anti-reflective nanocomposite based coating for crystalline silicon solar cells with noticeable significance. Journal of Renewable and Sustainable Energy 2013; 5(3): 3557–3567.
75. Jana S, Das S, De D, *et al.* Diamond-like nanocomposite: a novel promising carbon based thin film as antireflection and passivation coating for silicon solar cell. Materials Research Express 2018; 5(2): 9.

Characterization and Application of Nanomaterials (2020) Volume 3 Issue 1
doi:10.24294/can.v3i1.875

REVIEW ARTICLE

Nano-composites and their applications: A review

Sajad Hussain Din[1]*, M. A. Shah[2], N. A. Sheikh[1], M. Mursaleen Butt[1]

[1]*Department of Mechanical Engineering, National Institute of Technology, Srinagar 190006, India. E-mail: Sajad_08phd12@nitsri.net*

[2]*P.G Department of Physics, Special Center for Nanosciences, National Institute of Technology, Srinagar (J&K) 191131, India.*

ABSTRACT

Nanocomposites are high performance materials which reveal rare properties. Nanocomposites have an estimated annual growth rate of 25% and fastest demand to be in engineering plastics and elastomers. Their prospective is so prominent that they are valuable in numerous areas ranging from packaging to biomedical applications. In this review, the various types of matrix nanocomposites are discussed highlighting the need for these materials, their processing approaches and some recent results on structure, properties and potential applications. Perspectives include need for such future materials and other interesting applications. Being environmentally friendly, applications of nanocomposites propose new technology and business opportunities for several sectors of the aerospace, automotive, electronics and biotechnology industries.

Keywords: Nanocomposites; Ceramic Matrix Nanocomposites; Metal Matrix Nanocomposites

ARTICLE INFO

Article history:
Received 27 January 2020
Received in revised form 23 February 2020
Accepted 25 February 2020
Available online 7 March 2020

1. Introduction

Nanocomposites are composites in which at least one of the phases demonstrates dimensions in the nanometre range[1,2]. The word nanotechnology is novel but the existence of functional devices and structures of nanometer dimensions is primitive. In the fourth century, Roman glassmakers were formulating glasses encompassing nanosized metals. Nanocomposite materials have materialized as appropriate substitutes to incredulous restrictions of micro-composites. They are also testified to be the resources of 21st century in the view of having design rareness and property groupings that are not found in conventional composites[3-5]. Nevertheless, they pose preparation challenges associated to the regulator of basic arrangement and stoichiometry in the nanocluster phase. Nanocomposites are high performance materials demonstrating rare property arrangements[6-8]. Their potential is so conspicuous that they are beneficial in numerous areas ranging from packaging to biomedical applications. In this paper, the various types of matrix nanocomposites are presented underlining the need for these materials. Their processing methods, structure, properties and potential applications are discussed[9,10].

Nanocomposites suggest rare properties that ascend from their small size, large surface area, and the relations of phases at their interfaces. They are striking for their prospective to develop performance of drugs, catalysts, biomaterials and other high value added materials. It has been reported that deviations in particle properties can be observed

when the particle size is less than a particular level, called 'the critical size[11,12]. As dimensions reach the nanometre level, interactions at phase interfaces become mostly enhanced. Additionally, unearthing of carbon nanotubes and their successive use to formulate composites demonstrating some of the unique carbon nanotubes related mechanical, thermal and electrical properties, added a new and fascinating dimension to this area. Currently, nanocomposites offer new technology and business opportunities for all zones of industry, in addition to being environmentally friendly[13-15].

2. Prospects of nano-composites

Nanocomposites offer an exceptionally extensive range of prospective applications from electronics, optical communications and biological systems to new materials. Many possible applications have been explored and many devices and systems have been considered. More potential applications and new devices are being proposed. It is evidently impossible to recapitulate all the devices and applications that have been studied. It is interesting to note that the applications of nanocomposites in diverse fields have clearly different demands, and thus face different challenges, which necessitate different approaches[16-18]. The reinforcements refract the crack and deliver connecting elements, deterring further opening of the crack. The integrated phase experiences and phase transition in conjunction with the volume increase introduced by the stress field of a propagating crack, contributing for the toughening and strengthening processes. The potential of ceramic matrix nanocomposites, chiefly the Al_2O_3/SiC system, was exposed by the revolutionary work of Niihara. The toughening mechanism was based on the crack-bridging role of the nanosized reinforcement. The merger of high strength nano-fibres into ceramic matrices has per-mitted the preparation of advanced nanocomposites with high toughness and superior failure character-istics compared to the sudden failures of ceramic materials[19,20].

Space mission projects implicate ultra-lightweight space-crafts. These spacecraft devices are mobile mechanical parts such as gyroscopes, gears, solar arrays, antennae, drives, sunshields, rovers, radars, solar concentrators, and reflector arrays. These parts will have to be manufactured from flexible, appropriate materials, which can be folded or packaged into small volumes. This is needed since the structure consisting of ultra-lightweight parts would be deployed mechanically into a large ultra-lightweight functioning. It is imperative that the above mentioned characteristics should be available in one single material. Similarly, rocket propellants are prepared from a polymer-Al/Al_2O_3 nanocomposite to improve ballistic performance[21-23].

2.1 Processing of nanocomposites

Ceramic metallic nanocomposite matrix materials include Al_2O_3, SiC, SiN, etc., while metal matrices employed in metal matrix nanocomposites are mainly Al, Mg, Pb, Sn, W and Fe, and a whole range of polymers, e.g. vinyl polymers, condensation polymers, polyolefins, and speciality polymers are used in polymer matrix nanocomposites. Both synthetic and natural crystalline reinforcements have been used, such as Fe and other metal powders, clays, silica, TiO_2 and other metal oxides. Similarly, carbon nanotubes are prepared mostly by chemical/vapour deposition methods. In the case of carbon nanotubes, use of surfactants, oxidation or chemical functionalization of surfaces is some of the techniques employed. Physical blending and in-situ polymerization are used for improving dispersion in the case of carbon nanotube-reinforced polymer composites, while alignment of carbon nanotubes could be achieved by techniques such as ex-situ techniques[24,25].

2.2 Structure and properties of nanocomposites

The structure of nanocomposites consists of the matrix materials, containing the nanosized reinforcement components in the form of particles, whiskers, fibres, nanotubes, etc. Various techniques have been employed to characterize the nanocomposites, including atomic force microscopy (AFM), scanning tunnelling microscopy (STM), Fourier transformed infrared spectroscopy (FTIR), X-ray photoelectron spectroscopy (XPS), nuclear magnetic resonance (NMR), differential scanning calorim-

etry (DSC), scanning and transmission electron microscopy (SEM/TEM), etc. Simultaneous small angle X-ray scattering (SAXS) and X-ray diffractometry (XRD) studies have been recently used for quantitative characterization of nanostructures and crystallite structures in some nanocomposites[26-28].

Briefly, the density of single walled carbon nanotubes is less than one sixth of that of steel while the density of multi walled carbon nanotubes is one half of that of Al. Tensile strengths of single walled carbon nanotube and multi walled carbon nanotubes are reported to be in a range much higher than of high strength steel, while Young's modulus values are comparable to those of diamond. They exhibit tremendous resilience, in that they can sustain bending to large angles and restraightening without damage, in which they differ from the plastic deformation of metals and the brittle fracture of carbon fibres. Similarly, theoretical thermal and electrical conductivities are comparable with that of diamond, with an almost negligible thermal expansion coefficient. They also exhibit high thermal stability both in air and in vacuum, compared to the lower values obtained for metal wires in microchips, and high parallel and perpendicular magnetic susceptibilities[29-30].

2.3 Ceramic matrix nanocomposites (CMNC)

The most common methodologies for preparation of CMNC, are conventional powder method, polymer precursor route, spray pyrolysis, vapour techniques and chemical methods, which include the sol-gel process, colloidal and precipitation approaches and the template synthesis. Ceramics are usually brittle and easily fractured as consequence of crack propagation. Ceramics are made suitable for engineering applications through the incorporation of a ductile metal phase or another ceramic into the matrix. This leads to improved mechanical properties such as hardness and fracture toughness, which occur as a result of the relationship between the different phases, matrix and reinforcements, at the phase boundaries[31,32].

3. Ceramic matrix-discontinuous reinforcement nanocomposite systems

There is a significant improvement in the strength of the nanocomposite compared with its micro-counterpart. The fracture strength is noticeably higher because of the higher interfacial interaction between the particles in nanocomposites. Besides, Al_2O_3-5 to 15% SiC systems exhibited superficial grooves of plastic deformation compared to the intergranular fracture observed in monolithic materials. Furthermore, at 1673 K and tension of 200 MPa, Si_3N_4 fails after 0.4 hours at 0.3% strain, whereas the Si_3N_4/10% SiC nanocomposite does not fail even after 1,000 hours at 1.5% strain. Coming to morphological studies, microstructures of some ceramic matrix nanocomposites of Al_2O_3 and Fe_2O_3 contain a good distribution of Co and Ni nano-particles[33,34].

3.1 Ceramic matrix-carbon nanotube systems

When the volume content of carbon nanotubes is lower than 5 vol. %, both bending strength and fracture toughness increase with increasing volume of carbon nanotubes. However, loadings higher than 5% cause decrease in these two properties. At 5 vol. %, the increment in strength and fracture toughness, compared with that of monolithic SiO_2, is up to 65 and 100%, respectively. This increase in mechanical properties is due to the large aspect ratio and excellent mechanical properties of carbon nanotubes, according to the theory of short fibre-reinforced composites[35-37]. The decrease in bending strength at high loading is due to the limitation caused by carbon nanotubes during densification, as they express a higher probability for agglomeration. Also, the higher the loading of carbon nanotubes, the higher is their pull out from the matrix during stress transfer. Unusual behaviours such as high contact-damage resistance without a corresponding enhancement in toughness have also been reported in Al_2O_3/nanotube composites. The micro-hardness of these systems increases as the carbon nano-tube content is increased up to 4 wt. (%). This is probably due to grain size effects and the rein-forcement role of carbon nanotubes. As the carbon nanotube content increased above 10 wt. (%), wear losses also notably increased[38-40].

Preparation of SiC/carbon nanotubes showed a 10% upgradation in the strength and fracture toughness as compared to the monolithic ceramics. These results were attributed to nanotube/matrix debonding and crack deflection. As a consequence, many attempts have been made to improve mechanical properties through the incorporation of carbon nanotubes in ceramic matrices. However, the detected improvements were not as intense as expected. Single walled carbon nanotubes applied in the reinforcement of ceramic composites through spark-plasma sintering, resulted in a 194% increase in fracture toughness over pure alumina. A 24% increase in fracture toughness over the matrix was observed in nanograined Al_2O_3 composite containing 10 vol. % multi walled carbon nanotubes, which was attributed to the oxidation of carbon nanotubes before dispersion. In this case, the material was produced in three conditions, viz., mixed, hot pressed (1573 K) and sintered to near theoretical density[41-43].

3.2 Metal Matrix Nanocomposites (MMNC)

The discovery of new alloys has been escorted by major developments. The bronze was initiated by the discovery that intimate mixing of copper and tin, yielded a much stronger metal than copper. Regardless of methods of synthesis, most nanocrystalline based metal-metal nanocomposites exhibit a remarkable resistance to grain growth. Thermal stability and the mechanisms involved in nanocrystalline materials are not only related to the microstuctural and compositional parameters but also associateed to porosity, impurity, grain size distribution, texture and microstrain resulted during the processing of nanocrystalline materials. The simple mixing of two different metal nanocomposites will transpire with new properties. Nanocomposite systems such as carbon nanotubes, have been extensively studied. There has been a continuous increase in the number of publications on the subject, including reviews from time to time. In the case of PMNC, reviews deal with processing aspects, including those on layered silicates, conducting and biodegradable polymer-based systems, fibre reinforced structure, morphology and property aspects as well as with applications and perspectives, including key opportunities and challenges in the development of structural and functional fibre nanocomposites[44-46].

The techniques used for the processing of metal matrix-nanocomposites are spray pyrolysis, liquid metal infiltration, rapid solidification, vapour techniques, electrodeposition and chemical methods, which include colloidal and sol-gel processes. Fe-based nanocomposites are prepared by solidification techniques. Branagan stresses on “devitrified nanocomposite steel”. The formation of nano-phases was explained by the high nucleation frequency within the limited time for growth of grains before impingement. Use of ultrasound helped to improve the wettability between the matrix and the particles[47-48].

3.3 Metal–discontinuous reinforcement systems

The α-Fe/$Fe_{23}C_6$/Fe_3B system provides a good example of how unique properties may arise from metal nanocomposites. Vickers hardness values of these two forms of the alloy produced by Branagan and Tang were found to be 10.3 and 11 GPa in the assolidified condition. The ribbon variety showed increased hardness with increasing heat treatment temperature, showing a maximum of 16.2 GPa at 973 K and there after decreasing to 10.5 GPa at 1123 K. This can be compared to the decreasing trend of the ingot type (8 and 6.6 GPa at 873 and 973 K respectively). The Al/SiC system also illustrates the advantages of metal nano-composites compared to their micro counterparts. There is a linear increase in hardness with increasing volume fraction of the harder phase (SiC) until the maximum value of 2.6 GPa for the sample that contains 10 vol. % of SiC. The values of Young’s and shear modulus increase significantly with increasing SiC content, suggesting the formation of a nanocomposite material containing a brittle phase (SiC) embedded in the ductile Al matrix. Al/SiC nanocomposite exhibits notably higher Young’s modulus and hardness than its micro counterpart. For example, the nanocomposite shows 12.6% increase in hardness and 105.1% in Young’s modulus. Also, Al/Pb nanocomposites exhibit improved frictional fea-

tures[49-51].

4. Metal matrix-carbon nanotube composites

Electrical properties of an Al/carbon nanotube system measured between 4.2 K and room temperature revealed an increase from 4.9 to 6.6 μΩ cm at room temperature for 1 and 4 wt. (%) carbon nanotubes, but a decrease to 5.5 μΩ cm for 10 wt. (%) carbon nanotube), compared to the value of 3.4 μΩ cm for the Al matrix. At lower temperatures, resistivity of all composites decreased linearly, as in the case of metals, with an abrupt drop of about 90%. On the other hand, compression testing of these Al-carbon nanotube composites exhibited identical stress strain curves for both the composite without the precursor and pure Al, except for large elastic strain, while those with the precursor, though similar in shape, exhibited increased compression stresses. At a higher multi walled carbon nanotube loading (1.6 vol. %), proof stress increased seven fold, in contrast to a not so significant enhancement in polymer-carbon nanotube composites. The enhanced mechanical property has been attributed to the confinement of the Al matrix by the multi walled carbon nanotubes on nanoscale[52-55].

4.1 Strengthening mechanisms in metal matrix-composites

Upon cooling, dislocations form at the reinforcement/matrix interface due to the thermal mismatch. The thermally induced dislocation punching results in indirect strengthening of the matrix. In age-hardenable matrix-materials, the thermally induced dislocations serve as heterogeneous nucleation sites for precipitate formation during the aging treatment[56,57].

4.2 Polymer matrix-discontinuous reinforcement (non-layered) nanocomposites

The reinforcing materials engaged in the fabrication of polymer nanocomposites can be categorized according to their dimensions. Examples comprise spherical silica, metal particles and semiconductor nanoclusters. The second kind of reinforcement is formed by nanotubes or whiskers, which contain two dimensions in the nanometre scale and one larger, forming an extended structure. Carbon nanotubes and cellulose whiskers, broadly studied as reinforcing nanofillers, can be included in this second category[58-60]. The third type of reinforcement is characterized by only one dimension in the nanometre range. In this group, the filler contains sheets one to a few nanometres thick and hundreds to thousands nanometres long. This family is called polymer-layered nano-composites. Many synthetic and natural crystalline hosts that are able, under specific conditions, to intercalate a polymer have been described. Examples include graphite, metal chalcogenides, clays, layered silicate and layered double hydroxides. Nanocomposites based on clay and layered silicates have been usually explored due to the handiness of clay starting materials and their eminent intercalation chemistry[61-63].

4.3 Polymer nanocomposites with layered reinforcements

Although the chemistry of polymers towards layered silicates has long been known, the field of polymer layered silicate nanocomposites has gained inspiring attention. Firstly, the results obtained on Nylon-6 (N6)/montmorillonite nanocomposites, which showed that a small concentration of layered silicate lead to notable changes in thermal and mechanical properties. Secondly, the observation by Vaia *et al.* is possible to melt-mix polymers with layered silicates, without the use of organic solvents. The incorporation of montmorillonite into a Nylon-6 matrix has led to a noteworthy enhancement in its mechanical properties. The Young's modulus (or tensile modulus), for example, of pure Nylon-6 (1.11 GPa) was strongly upgraded when the nanocomposite was formed. The Nylon-6/MMT with a filler content of 4.1 wt. (%) gave a value of 2.25 GPa, which corresponds to an increase of 102.7%. Also, regarding Nylon-6 nanocomposites, a strong interaction between matrix and silicate layers occurs via formation of hydrogen bonds. This behaviour can also be supported by propene-modified maleic anhydride (PP-MA)/LS nanocomposites[64-66].

Exfoliated Nylon-6 and intercalated PMMA nanocomposites exhibited a prodigious increase in

the stress at break. This can be due to the polar (PMMA) and ionic interactions (Nylon-6 grafted onto the layers) between the matrix and the silicate layers. This increase is larger in Nylon-6 nanocomposites. On the other hand, propylene-based nanocomposites displayed only a small enhancement in tensile stress, which can be explained by the lack of interfacial adhesion between non-polar PP and polar-layered silicates. However, addition of maleic anhydride-modified polypropylene to the polypropylene matrix has confirmed to be effective in the intercalation of the PP chains and the maintenance of the ultimate stress at a satisfactory level. This finding is attributed to the weak interactions at the polystyrene-clay interface. It is imperative to note that in previous compositions in which polar interactions were developed, strengthening at the filler matrix interface was observed. Usually, when LS are dispersed in thermoplastics such as PMMA, PS or PP, the elongation at break is reduced[67-70]. The reported decrease in elongation is from 150% in pure PP matrix, to 105% for a 6.9 wt. (%) non-intercalated clay micro-composite. On the other hand, in a nanocomposite filled with 5 wt. (%) silicate layers, the more noticeable drop was 7.5%. Conversely, this loss in eventual elongation did not occur in elastomeric epoxy or polyol polyurethane matrices. In these cases, introduction of the nanoclay in cross-linked matrices causes a rise of the elongation at break. While a drop in the elongation at break can be perceived for the conventional composite, a minor improvement in this property can be observed for the intercalated nanocomposite[71-73].

Finally, exfoliated nanocomposites exhibit a large increase in the elongation at break. This is probably due to the plasticizing effect of the galleries, their contribution to the formation of dangling chains and conformational effects at the clay-matrix interface. The combination of improved stiffness (Young's modulus), toughness (stress at break) and elasticity (strain at break) makes elastomeric nanocomposites suitable candidates for the generation of a new family of high performance materials. Polyimide is another example of a polymer matrix material showing an increase in both stress and elongation at break. For example, when filled with montmorillonite exchanged with hexadecylammonium, these properties increase with the filler loading at least up to 5 wt. (%). At higher filler contents, both properties drop towards values lower than those described for the filler-free matrix due to the formation of non-exfoliated aggregates which make these composites more brittle[74,75].

Another nanocomposite system studied in great detail is Nylon-6 protonated aminododecanoic acid, which has been studied for its impact resistance properties. The nanocomposite synthesized by in-situ intercalative poly-merization had its Izod impact strength reduced from 20.6 to 18.1 J/m compared with the pure matrix when 4.7 wt. (%) of nanoclay was incorporated. Charpy impact testing displayed a similar reduction from 6.21 kJ/m^2 to 6.06 kJ/m^2 for the 4.7 wt. (%) nanocomposite. There is good resistance to impact, high Young's modulus, good flexural modulus and a notable enhancement in the heat distortion temperature, going from 338 K for pure Nylon-6 to more than 423 K for the nanocomposite, have allowed this material to replace glass fibre-reinforced nylon or polypropylene in the production of timing belt covers of automotive engines[76-78].

5. Conclusions

Innovative technologies necessitate materials exhibiting unique properties and upgraded performance. Therefore, nanocomposites are appropriate materials to meet the developing demands arising from scientific and technologic advances. Processing methods for different types of nano-composites pose challenges, thus giving opportunities for researchers to overcome the problems faced with nanosized materials. They propose better performance over counterpart materials and are subsequently appropriate materials to overcome the restrictions of many presently prevailing materials and devices. Many applications previously exist. These materials have much potential in engineering field. Due to high mechanical properties, gas barrier, flame related properties, and the market for these materials have been projected in various sectors. Thus, all types of nano-composites offer opportuni ties and rewards, creating new world wide interest in these new materials.

References

1. Dalton AB, Collins S, Munoz E, *et al*. Super-tough carbon-nanotube fibres — These extraordinary composite fibres can be woven into electronic textiles. Nature 2003; 423(6941): 703–703.
2. Roy R, Roy RA, Roy DM. Alternative perspectives on "quasi-crystallinity": Non-uniformity and nanocomposites. Materials Letters 1986; 4(8-9): 323–328.
3. Ounaies Z, Park C, Wise KE, *et al*. Electrical properties of single wall carbon nanotube reinforced polyimide composites. Composites Science and Technology 2003; 63(11): 1637–1646.
4. Schmidt D, Shah D, Giannelis EP. New advances in polymer/layered silicate nanocomposites. Current Opinion in Solid State and Materials Science 2002; 6(3): 205–212.
5. Gleiter H. Materials with ultrafine microstructures: Retrospectives and perspectives. Nanostructured Materials 1992; 1(1): 1–19.
6. Iijima S. Helical microtubes of graphitic carbon. Nature 1991; 354(6348): 56–58.
7. Braun T, Schubert A, Sindelys Z. Nanoscience and nanotechnology on the balance. Scientometrics 1997; 38(2): 321–325.
8. Kamigaito O. What can be improved by nanometer composites? Journal of Japan Society of Powder Metalurgy 1991; 38(3): 315–321.
9. Biercuk MJ, Llaguno MC, Radosvljevic M, *et al*. Carbon nanotube composites for thermal management. Applied Physics Letters 2002; 80(15): 2767–2769.
10. Weisenberger MC, Grulke EA, Jacques D, *et al*. Enhanced mechanical properties of polyacrylonitrile/multiwall carbon nanotube composite fibers. Journal of Nanoscience and Nanotechnology 2003; 3(6): 535–539.
11. Choa YH, Yang JK, Kim BH, *et al*. Preparation and characterization of metal/ceramic nanoporous nanocomposite powders. Journal of Magnetism and Magnetic Materials 2003; 266(1-2): 12–19.
12. Wypych F, Seefeld N, Denicolo I. Preparation of nanocomposites based on the encapsulation of conducting polymers into 2H-MoS_2 and 1T-TiS_2. Quimica Nova 1997; 20(4): 356–360.
13. Aruna ST, Rajam KS. Synthesis, characterisation and properties of Ni/PSZ and Ni/YSZ nanocomposites. Scripta Materialia 2003; 48(5): 507–512.
14. Giannelis EP. Polymer layered silicate nanocomposites. Advanced Materials 1996; 8(1): 29–35.
15. Sternitzke M. Review: Structural ceramic nanocomposites. Journal of the European Ceramic Society 1997; 17(9): 1061–1082.
16. Peigney A, Laurent CH, Flahaut E, *et al*. Carbon nanotubes in novel ceramic matrix nanocomposites. Ceramic International 2000; 26(6): 677–683.
17. Alexandre M, Dubois P. Polymer-layered silicate nanocomposites: Preparation, properties and uses of a new class of materials. Materials Science & Engineering 2000; 28(1-2): 1–63.
18. Gangopadhyay R, De A. Conducting polymer nanocomposites: A brief overview. Chemistry of Materials 2000; 12(7): 608–622.
19. Pandey JK, Raghunatha Reddy K, Pratheep Kumar A, *et al*. An overview on the degradability of polymer nanocomposites. Polymer Degradation and Stability 2005; 88(2): 234–250.
20. Thostenson ET, Li C, Chou TW. Nanocomposites in context. Composites Science and Technology 2005; 65(3-4): 491–516.
21. Jordan J, Jacob KI, Tannenbaum R, *et al*. Experimental trends in polymer nanocomposites — A review. Materials Science and Engineering: A 2005; 393(1-2): 1–11.
22. Choi SM, Awaji H. Nanocomposites — A new material design concept. Science and Technology of Advanced Materials 2005; 6(1): 2–10.
23. Xie X, Mai YW, Zhou X. Dispersion and alignment of carbon nanotubes in polymer matrix: A review. Materials Science & Engineering: R 2005; 49(4): 89–112.
24. Ray SS, Bousmina M. Biodegradable polymers and their layered silicate nanocomposites: In greening the 21st century materials world. Progress in Materials Science 2005; 50(8): 962–1079.
25. Jitendra KP, Pratheep KA, Manjusri M, *et al*, Recent advances in biodegradable nanocomposites. Journal of Nanoscience and Nanotechnology 2005; 5(4): 497–526.
26. Awaji H, Choi SM, Yagi E. Mechanisms of toughening and strengthening in ceramic-based nanocomposites. Mechanics of Materials 2002; 34(7): 411–422.
27. Niihara K. New design concept of structural ceramics — Ceramic nanocomposite. Journal of the Ceramic Society of Japan 1991; 99(1154): 974–982.
28. Nakahira A, Niihara K. Strctural ceramic nanocomposites by sintering method: Role of nano-size particles [PhD thesis]. Osaka: Osaka University; 1991. p. 404–417.
29. Chang JH, An YU. Nanocomposites of polyurethane with various organoclays: Thermomechanical properties, morphology, and gas permeability. Journal of Polymer Science Part B Polymer Physics 2002; 40(7): 670–677.
30. Zavyalov SA, Pivkina AN, Schoonman J. Formation and characterization of metal-polymer nanostructured composites. Solid State Ionics 2002; 147(3-4): 415–419.
31. Thompson CM., Herring HM, Gates TS, *et al*. Preparation and characterization of metal oxide/polyimide nanocomposites. Composites Science and Technology 2003; 63(11): 1591–1598.
32. Liu TX, Phang IY, Shen L, *et al*. Morphology and mechanical properties of multiwalled carbon nanotubes reinforced nylon-6 composites. Macromolecules 2004; 37(19): 7214–7222.
33. Shah MA, Sheikh NA, Najar KA, *et al*. Influence of boron doping on mechanical and tribological properties in multilayer CVD-diamond coating system. Bulletin of Materials Science 2016, 39(7):

1753–1761.
34. Ogawa M, Kuroda K. Preparation of inorganic-organic nanocomposites through intercalation of organoammonium ions into layered silicates. Bulletin of the Chemical Society of Japan 1997; 70(11): 2593–618.
35. Kojima Y, Usuki A, Kawasumi M, *et al*. Mechanical properties of nylon 6-clay hybrid. Journal of Materials Research 1993; 8(5): 1185–1189.
36. Stearns LC, Zhao J, Harmer MP. Processing and microstructure development in Al_2O_3-SiC 'nanocomposites'. Journal of the European Ceramic Society 1992; 10(6): 473–477.
37. Borsa CE, Brook RJ. Fabrication of Al_2O_3/SiC nanocomposites using a polymeric precursor for SiC. In: Hausner H, Messing GL, Horano S (editors). Proceedings of the International Conference of Ceramic Processing Science and Technology; 1994 Sept. 11-14; Friedrichshafen. Westerville, Germany: The American Ceramic Society; 1995. p. 653–658.
38. Riedel R, Strecker K, Petzow G. In situ polysilane-derived silicon carbide particulates dispersed in silicon nitride composite. Journal of the American Ceramic Society 1989; 72(11): 2071–2077.
39. Riedel R, Seher M, Becker G. Sintering of amorphous polymer-derived Si, N and C containing composite powders. Journal of the European Ceramic Society 1989; 5(2): 113–122.
40. Din SH, Shah MA, Sheikh NA. Tribology in industry effect of CVD-diamond on the tribological and mechanical performance of Titanium Alloy (Ti_6Al_4-V). Tribology in Industry 2016; 38(4): 530–542.
41. Vorotilov KA, Yanovskaya MI, Turevskaya EP, *et al*, Sol-gel derived ferroelectric thin films: Avenues for control of microstructural and electric properties. Journal of Sol-Gel Science and Technology 1999; 16(1-2): 109–118.
42. Hench LL, West JK. The sol-gel process. Chemical Review 1990; 90(1): 33–72.
43. Ennas G, Mei A, Musinu A, *et al*. Sol-gel preparation and characterization of Ni-SiO_2 nanocomposites. Journal of Non-Crystalline Solids 1998; 232-234: 587–593.
44. Sen S, Choudharya RNP, Pramanik P. Synthesis and characterization of nanostructured ferroelectric compounds. Materials Letters 2004; 58(27-28): 3486–3490.
45. Viart N, Richard-Plouet M, Muller D, *et al.* Synthesis and characterization of Co/ZnO nanocomposites: Towards new perspectives offered by metal/piezoelectric composite materials. Thin Solid Films 2003; 437(1-2): 1–9.
46. Kundu TK, Mukherjee M, Chakravorty D, *et al*. Growth of nano-α-Fe_2O_3 in a titania matrix by the sol-gel route. Journal of Matererials Science 1998; 33(7): 1759–1763.
47. Baiju KV, Sibu CP, Rajesh K, *et al*. An aqueous sol-gel route to synthesize nanosized lanthana-doped titania having an increased anatase phase stability for photocatalytic application. Materials Chemistry and Physics 2005; 90(1): 123–127.
48. Ananthakumar S, Prabhakaran K, Hareesh US, *et al*. Gel casting process for Al_2O_3-SiC nanocompositees and its creep characteristics. Materials Chemistry and Physics 2004; 85(1): 151–157.
49. Sivakumar S, Sibu CP, Mukundan P, *et al*. Nanoporous titania-alumina mixed oxides — An alkoxide free sol-gel synthesis. Materials Letters 2004; 58(21): 2664–2669.
50. Warrier KGK, Anilkumar GM. Densification of mullite-SiC nanocomposite sol-gel precursors by pressureless sintering. Materials Chemistry and Physics 2001; 67(1-3): 263–266.
51. Wunderlich W, Padmaja P, Warrier KGK. TEM characterization of sol-gel-processed alumina–silica and alumina–titania nano-hybrid oxide catalysts. Journal of the European Ceramic Society 2004; 24(2): 313–317.
52. Camargo PHC, Satyanarayana KG, Wypych Fernando. Nanocomposites: Synthesis, structure, properties and new application opportunities. Materials Research 2009; 12(1): 1–39.
53. Yu M, Lourie O, Moloni K, *et al*. Strength and breaking mechanism of multiwalled carbon nanotubes under tensile load. Science 2000; 287(5453): 637–640.
54. Novoselov KS, Geim AK, Morozov SV, *et al.* Two-dimensional gas of massless dirac fermions in graphene. Nature 2005; 438(7065): 197–200.
55. Dresselhaus MS, Dresselhaus G. Intercalation compounds of graphite. Advances in Physics 2002; 51(1): 1–186.
56. Hirata M, Gotou T, Horiuchi S, *et al*. Thin-film particles of graphite oxide 1: High-yield synthesis and flexibility of the particles. Carbon 2004; 42(14): 2929–2937.
57. Novoselov KS, Geim AK, Morozov SV, *et al*. Electric field effect in atomically thin carbon films. Science 2004; 306(5696): 666–669.
58. Zhang Y, Small JP, Amori MES, *et al*. Electric field modulation of galvanomagnetic properties of mesoscopic graphite. Physical Review Letters 2005; 94(17): 176803.
59. Berger C, Song Z, Li T, *et al*. Ultrathin epitaxial graphite: 2D electron gas properties and a route toward graphene-based nanoelectronics. The Journal of Physics Chemistry B 2004; 108(52): 19912–16.
60. Stankovich S, Piner R, Chen X, *et al*. Stable aqueous dispersions of graphitic nanoplatelets via the reduction of exfoliated graphite oxide in the presence of poly (sodium 4-styrenesulfonate). Journal of Materials Chemistry 2006; 16: 155–158.
61. Stauffer D, Aharnoy A. Introduction to Percolation Theory. Bristol: Taylor and Francis; 1991. p. 181.
62. Ounaies Z, Park C, Wise KE, *et al*. Electrical properties of single wall carbon nanotube reinforced polyimide composites. Composites Science and Technology 2003; 63(11): 1637–1646.
63. Chung DDL. Electrical applications of carbon materials. Journal of Materials Science 2004; 39: 2645–2661.
64. Vaia RA, Wagner HD. Framework for nanocomposites. Materials Today 2004; 7(11): 32–37.

65. He H, Klinowski J, Forster M, *et al*. A new structural model for graphite oxide. Chemical Physics Letters 1998; 287(1-2): 53–56.
66. Zhang Y, Tan Y, Stormer HL, *et al*. Experimental observation of the quantum hall effect and Berry's phase in graphene. Nature 2005; 438: 201–204.
67. Lerf A, He H, Forster M, *et al*. Structure of graphite oxide revisited. The Journal of Physics Chemistry B 1998; 102(23): 4477–4482.
68. Hirata M, Gotou T, Ohba M. Thin-film particles of graphite oxide. 2: Preliminary studies for internal micro fabrication of single particle and carbonaceous electronic circuits. Carbon 2005; 43(3): 503–10.
69. Kovtyukhova NI, Ollivier PJ, Martin BR, *et al*. Layer-by-layer assembly of ultrathin composite films from micron-sized graphite oxide sheets and polycations. Chemistry of Materials 1999; 11(3): 771–778.
70. Kotov NA, Dekany I, Fendler JH. Ultrathin graphite oxide-polyelectrolyte composites prepared by self-assembly: Transition between conductive and non-conductive states. Advanced Materials 1996; 8(8): 637–641.
71. Szabo T, Szeri A, Dekany I. Composite graphitic nanolayers prepared by self-assembly between finely dispersed graphite oxide and a cationic polymer. Carbon 2005; 43(1): 87–94.
72. Jiang M, Dai L. Shear-band toughness of bulk metallic glass. Acta Materialia 2011; 59(11): 4525–37.
73. Cassagneau T, Guerin F, Fendler JH. Preparation and characterization of ultrathin films layer-by-layer self-assembled from graphite oxide nanoplatelets and polymers. Langmuir 2000; 16(18): 7318–7324.
74. Huang R, Suo Z, Prevost JH, *et al*. Inhomogeneous deformation in metallic glasses. Journal of the Mechanica and Physics of Solids 2002; 50(5): 1011–27.
75. Du X, Xiao M, Meng Y, *et al*. Novel synthesis of conductive poly(arylene disulfide)/graphite nanocomposite. Synthetic Metals 2004; 143(1): 129–132.
76. Grady DE. Properties of an adiabatic shear-band process zone. Journal of The Mechanics and Physics of Solids 1992; 40(6): 1197–1215.
77. Kocks UF, Mecking H. Physics and phenomenology of strain hardening: the FCC case. Progress in Materials Science 2003; 48(3): 171–273.
78. Spaepen F. A microscopic mechanism for steady state inhomogeneous flow in metallic glasses. Acta Metallurgica 1977; 25(4): 407–415.

Characterization and Application of Nanomaterials

Focus and Scope

Characterization and Application of Nanomaterials is an international open access journal that publishes original research articles and review articles related to all areas of nanomaterials.

This journal covers modeling, simulation, nanotechnology, thin film, fabrication, synthesis and properties of nanomaterials.

EnPress Publisher, LLC

EnPress Publisher, LLC, is a scholastic conduit for an assembly of professionals in the domains of science, technology, medicine, engineering, education, social sciences and many more, as a roundtable for their intellectual discourse and presentation, and as an instrument to galvanize research designs, policy implementation and commercial interests, to facilitate the prevailing over their challenges and to encourage to the full advantage of their resources and true potential.

We are the intellectual and academic home for academic, educators, scholars, clinicians, corporate researchers, who all play important roles in a wide range of national and international research organisations, and whose interests, expertise, research approaches and industry objectives from around the world coalesce together to advance significant contributions in their research and professional fields.

As an instrument of information purveyor, we seek to combine academic rigor and originality with the nuanced development of policy and practice. Via our journals, client database, online campaigns and social media presence, we offer a platform for industry professionals to interconnect, as well as opening doors towards cost-effective solutions for them to succeed, and we confidently hope to inspire a new generation of multidisciplinary researchers, think-tank experts, policymakers and business entities to innovate and advance their knowledge across fields.

EnPress Publisher,LLC

Add 14701 Myford Road,Suite B-1,Tustin,CA 92780,United States

Tel +1（949）299 0192

Emali contact@enpress-publisher.com

Web https://enpress-publisher.com